

## **Spatial Variations in Isostatic Compensation Mechanisms of the Ninetyeast Ridge and their Tectonic Significance**

**K.M. Sreejith<sup>1</sup>, K.S. Krishna<sup>2\*</sup>**

<sup>1</sup> Geosciences Division, Marine, Geo and Planetary Sciences Group, Space Applications Center (ISRO), Ahmedabad, India - 380015

<sup>2</sup> CSIR - National Institute of Oceanography, Dona Paula, Goa, India – 403004

\* Corresponding Author's E-mail: krishna@nio.org

### **Abstract**

The Ninetyeast Ridge (NER), one of the longest linear volcanic features on the Earth, offers an excellent opportunity of understanding the isostatic response to the interactions of mantle plume with the migrating mid-ocean ridge. Bathymetry, geoid and gravity (ship-borne and satellite) data along 72 closely spaced transects and 17 overlapping grids on the NER are analyzed and modeled to determine the effective elastic thickness ( $Te$ ) beneath the entire ridge. The results of 2-D and 3-D flexural modeling of the NER show large spatial variations in  $Te$  values ranging from 4 to 35 km, suggesting that the ridge was compensated along its length by different isostatic mechanisms. The southern (south of 22°S latitude) and northern (north of 2°N latitude) parts of the NER have  $Te$  values of >10 and >23 km, respectively, revealing that the southern part was emplaced on a lithosphere of intermediate strength possibly on flank of the Indian plate, whereas the northern part was emplaced in an intraplate setting. In contrast, in the central part of the NER (between latitudes 22°S and 2°N), highly variable  $Te$  values (4 - 22 km) are estimated. The scattered  $Te$  values in the central NER suggest that this part may have evolved due to the occurrence of more frequent ridge jumps caused by the interaction of Kerguelen hot spot with rapid northward migration of the Wharton spreading ridge. Residual Mantle Bouguer Anomaly (RMBA) map of the NER and adjacent basins reveals that the entire length of the NER is associated with a significant negative anomaly up to 200 mGal, indicating the presence of thickened crust or less dense mantle beneath the ridge. 3-D crustal thickness map of the NER, generated by inversion of the RMBA data, shows a thick crust ranging from 15 to 19 km. The present study clearly shows that NER possesses a highly segmented isostatic pattern with the occurrence of sub-crustal underplating or sub-surface loading.

**Keywords:** Ninetyeast Ridge, Crustal structure, Isostasy, Effective elastic thickness, Ridge jumps

## 1. Introduction

During the Cretaceous period the Earth witnessed several major magmatic events resulting in the formation of numerous plateaus and linear seamount chains or ridges in the World's oceans. The Hawaii-Emperor Chain and Louisville Ridge in the Pacific Ocean, Walvis Ridge in the Atlantic Ocean and Ninetyeast Ridge (NER) in the Indian Ocean are the best examples of traces of long-lived mantle plume activities. The hot spot tracks provide excellent opportunities for understanding the process of ridge-hot spot interactions, migration of mid-ocean ridge systems, ridge jumps, motion of hot spots, lithospheric response to the surface and subsurface volcanic loads, etc. The NER, probably the longest linear feature on Earth, extends for more than 5000 km roughly along the 90°E meridian between 30°S and 17°N latitudes in the eastern Indian Ocean (Figure 1). It is generally accepted that the NER was emplaced on the Indian plate when it was moved northward over the Kerguelen hot spot during the period 82-38 Ma following the formation of Rajmahal traps on the Indian subcontinent, Bunbury basalts on the Australian continent, Broken Ridge, and southern and central parts of the Kerguelen Plateau [Peirce, 1978; Duncan, 1991; Coffin *et al.*, 2002]. Presently the NER intersects the E-W trending Broken Ridge in south, whereas in the Bay of Bengal (north of 10°N) the ridge is buried entirely under thick Bengal Fan sediments [Curry *et al.*, 1982; Gopala Rao *et al.*, 1997; Michael and Krishna, 2011]. Bathymetry and seismic studies reveal that the NER has an average width of 200 km and relief of more than 2 km with asymmetric margins [Sclater and Fisher, 1974; Fisher *et al.*, 1982; Krishna *et al.*, 1995, 2001a; Sager *et al.*, 2013]. Further, the NER is experiencing the intraplate deformation activity currently occurring within the Indo-Australian plate [Sager *et al.*, 2013] and separates the compressional deformation of the Central Indian Basin [Bull and Scrutton, 1992; Krishna *et al.*, 2001b, 2009] from the strike-slip dominated deformation of the Wharton Basin [Deplus *et al.*, 1998].

New geochronology data of core samples from the DSDP Sites 216, 214, 254 and ODP Sites 758, 756 along the NER suggest linear age progression from north (77 Ma at ODP Site 758) to south (43 Ma at DSDP Site 254) [Pringle *et al.*, 2008], and the age trend further strengthens the hot spot hypothesis for origin of the ridge. Though the age progression along the NER seems to be remarkably linear, the ocean basins adjacent to the NER include complex magnetic anomaly progressions (Figure 2) caused by cessation of spreading ridge segments at different ages [Sclater and Fisher, 1974; Royer and Sandwell, 1989; Royer *et al.*, 1991; Krishna *et al.*, 1995, 1999]. Geochronology data along the NER [Pringle *et al.*, 2008] and magnetic patterns in adjacent Central Indian and Wharton basins [Krishna *et al.*, 2012] reveal that the NER was emplaced at a rate of 118

km/Myr, which is almost double the accretion rate (48-58 km/Myr) of the adjacent ocean floor. Higher accretion rate of the ridge that contributed to the lengthening of the NER, was explained by frequent southward jumps of the Wharton spreading ridge segments toward the hot spot, which transferred portions of crust from the Antarctic plate to the Indian plate [Krishna *et al.*, 2012]. One important aspect yet to be understood is the long-term response of the oceanic lithosphere to volcanic loads on a migrating mid-ocean ridge and frequent southward ridge jumps for more than 40 Myr.

In this study, we examine the possibility of using variation of isostatic compensation mechanisms along the ridge as a proxy to the ridge-hot spot interactions. Previously, the NER's isostasy was examined using 2-D admittance analysis of ship-borne bathymetry and gravity data [Detrick and Watts, 1979; Grevemeyer and Flueh, 2000] which suggested local compensation mechanism beneath the ridge. Detrick and Watts [1979] computed the admittance by averaging 14 bathymetry and gravity profiles from equator to about 25°S, whereas Grevemeyer and Flueh [2000] used a single profile along 17°S for the analysis. Subsequently, Tiwari *et al.* [2003] have studied the variations in  $T_e$  values derived from 3-D admittance analysis of satellite-derived gravity and bathymetry grids of nine non-overlapping rectangular blocks from 30°S to 10°N along the ridge. However, we feel that detailed analyses of 2-D and 3-D flexural modeling studies and characterization of crustal structure beneath the entire length of the ridge are needed to better understand the spatial variations in compensation mechanisms of the ridge.

In the present study, we investigate the variations in isostatic compensation mechanisms along the entire NER using flexural modeling of ship-borne and satellite gravity, bathymetry and geoid data. 2-D flexural modeling along 72 profiles of ship-borne as well as satellite-derived gravity, bathymetry and residual geoid data across the NER from 28°S to 8°N was carried out to constrain finer variations in  $T_e$  along the NER. Further, 3-D flexural modeling using satellite-derived gridded data sets from 17 overlapping blocks was used to constrain  $T_e$  estimates along the NER. In addition, 3-D crustal structure of the NER has also been derived using inversion of Residual Mantle Bouguer Anomaly (RMBA) data. The major objectives of this study are 1) to determine the  $T_e$  values along the entire length of the NER using 2-D and 3-D flexural modeling; 2) to determine the crustal structure and investigate the isostatic compensation mechanisms of the ridge using 3-D gravity inversion; 3) to examine the spatial variations in  $T_e$  values along the ridge in light of complex interactions that occurred between the Kerguelen hot spot and migrating Wharton spreading ridge system.

## 2. Analyses of Bathymetry, Gravity, Geoid and Sediment thickness data of the NER

Bathymetry and ship-borne gravity profiles crossing the NER were chosen from the geophysical database of the eastern Indian Ocean compiled from different oceanographic cruises of Indian and Russian research programs and as well from NGDC. In order to have a 50 km spacing interval along the entire length of the ridge, larger gaps between the locations of ship-borne profiles were filled in with 54 bathymetry [Smith and Sandwell, 1997] and satellite-derived gravity [Sandwell and Smith, 2009] profiles (Figure 1). The Smith and Sandwell bathymetry grid was derived by limiting the waveband to avoid wavelengths where  $T_e$  is important and then adjusting the predictions to coincide with the ship-borne bathymetry along surveyed points [Smith and Sandwell, 1997]. Earlier, Rapp [1998] found that accuracy of satellite gravity data is fairly good in deep ocean regions, therefore it is considered that the data resolve the signatures associated with the geological features having wavelengths as low as 23 km [Marks, 1996]. The reliability of satellite-derived gravity data in the study area is tested by comparing with several ship-borne gravity profiles. Both the datasets match very well with an average RMS error of 4.4 mGal.

The seafloor morphology of the NER all along its length (Figures 1 and 2) is quite variable. As noticed previously [Sclater and Fisher, 1974; Krishna *et al.*, 1995, 2001a; Sager *et al.*, 2010, 2013], south of 10°S the ridge feature is prominent and continuous with an average width and relief of 200 km and 3 km, respectively. The NER segment between 10°S and equator has distinct morphology of isolated rises with a narrow width of ~100 km. North of the equator the ridge consists of relatively wider en-echelon blocks traceable up to 10°N; and further north the ridge continues into the Bay of Bengal up to 17°N under the thick Bengal Fan sediments [Curry *et al.*, 1982; Gopala Rao *et al.*, 1997; Michael and Krishna, 2011]. The NER is often asymmetric as seen in seismic cross sections, for example on eastern flank of the south part of NER, a steep scarp fault with a throw of more than 2 km is observed [Krishna *et al.*, 1995, 2001a]. In contrast, the central part of the ridge is faulted on its western flank.

Recently, Sreejith *et al.* [2013] have updated the residual geoid map of the north Indian Ocean by subtracting the EGM2008 geoid model up to degree and order 50 from the altimeter derived geoid. The EGM2008 geoid coefficients are smoothly rolled off between degrees 30-70 in order to avoid artifacts related to the sharp truncation at degree 50. This corresponds to cosine tapering for wavelengths between 571 and 1332 km. These wavelengths were selected in order to isolate the geoid anomaly components corresponding to lithospheric flexure from the one associated with deep processes such as mantle convection. From this database, a geoid anomaly map of the NER is

prepared (Figure 3); the data range from 0 to 4 m and show excellent correspondence with the seafloor topography of the ridge. The Andaman Subduction Zone is clearly marked with bi-polar geoid anomalies - geoid high parallel to the arc and geoid low following the location of trench. It is also observed that, unlike the gravity data, shallow basement features such as fracture zones are not clearly seen in the geoid map. In order to correct the bathymetry and gravity data over the northern part of the NER (2°N to 8° N) we have prepared and used sediment thickness maps of the ridge by combining the information available from *Levchenko et al.* [1993], *Curray* [1994] and a world sediment thickness map [*Divins*, 2009].

### **3. Calculation of Residual Mantle Bouguer Anomaly (RMBA) and Residual Topography of the NER**

The Mantle Bouguer Anomaly (MBA) data of the NER are generated from the free-air gravity anomaly data of the ridge by subtracting the attraction of sediments, seafloor topography, and crust-mantle interface assuming an average 6 km thick crust. Residual Mantle Bouguer Anomaly (RMBA) is calculated by removing the gravity effects of cooling lithosphere and age-dependent subsidence from the MBA and is shown in Figure 4. We considered an updated version of global age grid of *Mieller et al.* [1997] and age-depth relation of *Stein and Stein* [1992] as reference models for the calculations. The MBA and RMBA computations were carried out using an algorithm developed by *Parker* [1972]. The *Stein and Stein* [1992] subsidence trend was removed from the bathymetry to compute the residual topography. The residual topography is scaled with respect to the shallowest point in the map as reference.

The RMBA data, in general, reflect the deviations in crustal thickness from a 6 km normal oceanic crust and/or upper mantle density distributions. The RMBA map of the NER (Figure 4) reveals that the southern part of the ridge is associated with more prominent negative anomalies, reaching magnitudes up to -200 mGal. The width of the RMBA of the ridge is much larger than that of the free-air gravity anomalies.

### **4. Effective Elastic Thickness ( $T_e$ ) along the NER**

#### **4.1 Flexural modeling**

Gravity and residual geoid data observed at the sea surface are sensitive to both topographic loads and deflections at the Moho boundary. The relationship between the topographic loads and

underlying Moho deflections as well as the gravity response to each can be described in the Fourier Domain considering the elastic plate approximations [Watts, 1978; Watts, 2001] as

$$\Delta g(k) = 2\pi G(\rho_l - \rho_w)e^{-kd}(1 - \phi_e(k)e^{-kt})H(k) \quad (1)$$

Similarly the expression for geoid response could be written as

$$\Delta T(k) = \frac{2\pi G(\rho_l - \rho_w)e^{-kd}}{gk}(1 - \phi_e(k)e^{-kt})H(k) \quad (2)$$

where,  $\Delta g(k)$ ,  $\Delta T(k)$  and  $H(k)$  represent Fourier transforms of gravity anomaly, geoid and topography, respectively and  $\phi_e(k) = \left[1 + \frac{Dk^4}{g(\rho_m - \rho_c)}\right]^{-1}$ .  $D$  is the flexural rigidity and is related to

$Te$  as

$$D = \frac{ETe^3}{12(1 - \nu^2)} \quad (3)$$

The parameters in the above expressions are described in Table 1.

In flexural modeling the gravity and geoid effect of the bathymetry and its compensation is computed for a range of  $Te$  values, and the computed geoid and gravity anomalies are compared with the observed anomalies. Traditionally the best fitting  $Te$  is considered based on the minimum RMS error criteria. Analyses of several profiles along the NER reveal that the best fit  $Te$  is not tightly constrained by simple RMS error method as it does not contain information about the anomaly shape. Hence, we use an objective function as formulated by Smith *et al.* [1989], which combines the RMS error and correlation coefficient between observed and modeled gravity for determining the best fit  $Te$  values. The objective function is defined as

$$obfn = 0.5 \left[ \frac{RMS}{RMS_{\max}} + R^2 \right] \quad (4)$$

where,  $RMS_{\max}$  is the maximum RMS error of all models and  $R^2$  represents the correlation coefficient between the observed and modeled gravity anomaly. The upper and lower bounds of  $Te$  is determined using the intersection of the line defined by  $obfn_{\min} * (1 + x)$ , on the  $obfn$  curve, where  $x$  is the tolerance parameter defined as 5% of the  $obfn_{\min}$ . The model parameters used for the computations of flexural model are listed in Table 1.

We carried out 2-D flexural modeling of closely spaced 72 profiles to obtain finer variations in  $T_e$  beneath entire length of the NER. A total of 18 ship-borne and 54 satellite profiles of bathymetry and free-air gravity and residual geoid data crossing the NER between 28°S and 8°N with an interval of ~50 km were chosen for the flexural modeling. For the purpose of spectral estimations, bathymetry and gravity profiles were projected perpendicular to the strike of the ridge and their length is limited to 800 km keeping the ridge crest in the center. Short ship-borne gravity profiles were extended on either side to match the extent of satellite gravity profiles in order to maintain consistency. The data were interpolated at 2.2 km and the mean and linear trend were removed. The profile ends were tapered using a cosine window of 10% profile length prior to the spectral estimation.

Theoretically, 2-D modeling of 3-D geological feature is based on the assumption that the feature is infinitely long and the profile is perpendicular to the feature. However, by thumb rule, the length of the feature should be >250 km for safe assumption of two-dimensionality [Ribe, 1982]. Incorrect assumptions of two-dimensionality for 3-D features such as individual seamounts may lead to considerable errors in  $T_e$  estimates [Lyons *et al.*, 2000]. In order to overcome these errors in  $T_e$  estimation, 3-D flexural modeling was also carried out using gridded bathymetry, gravity and residual geoid data in 17 overlapping blocks along the NER. The size of each block is selected as 550 km x 550 km and the recovered  $T_e$  is assigned to the center of the block.

$T_e$  values obtained from both 2-D and 3-D flexural modeling using bathymetry-FAA and bathymetry-residual geoid data are summarized in Tables 2 and 3, respectively and presented in Figure 5.  $T_e$  values determined by 2-D flexural modeling at 50 km interval along the ridge reveal finer details in  $T_e$  values associated with the NER, whereas 3-D modeling results reveal average  $T_e$  value at every 200 km along the ridge. Both 2-D and 3-D model studies show similar trend and magnitude of  $T_e$  estimates. The average difference between the best-fit  $T_e$  estimated using both data sets are about 1.5 km for 2-D method and about 1 km for 3-D method. The best-fit  $T_e$  and its error limits for each profile or block is assigned as the average value of  $T_e$  determined using bathymetry-FAA and bathymetry-residual geoid data. The overall parabolic trend of the curve, in general, suggests that the central part of the ridge (between 21°S and 2°N) is associated with low  $T_e$  values with some scattered highs, whereas the northern and southern parts are associated with relatively higher  $T_e$  values (Figure 5).  $T_e$  values obtained from 2-D flexural modeling suggest that the southern part of the NER (between 22°S and 28°S) is associated with  $T_e$  values of 10-14 km. In the central part, the  $T_e$  values are extremely variable (4-22 km). The southern part is separated from the central part with a discontinuity in  $T_e$  trend between 21°S and 18°S. A careful examination of the pattern of

$T_e$  values in the central part suggests two distinct features, in south-central part between 18°S and 8°S,  $T_e$  values nearly linearly decrease from 20 km to 5 km, while in north-central part between 8°S and 2°N,  $T_e$  values are extremely variable ranging from 4 to 22 km. The northern part of the ridge (north of 2°N) is associated with high  $T_e$  values of 23-35 km.

The results of 2-D flexural modeling carried out along eight selected profiles with the consideration of two profiles from each part of the NER are shown in Figures 6a-d. For profiles V1811, S8, A20931 and V3305 (Figures 6a-b), match between observed gravity/residual geoid and best-fit gravity/residual geoid is fairly good except along the eastern edge of the ridge. The exception could be due to the effect of the 89°E FZ bounding the eastern edge of the NER. Highly variable  $T_e$  values obtained along north-central part of the ridge is evident from the contrasting  $T_e$  values obtained along nearby profiles S39 ( $T_e=9$  km) and SK 28-4 ( $T_e=22$  km) (Figure 6c). The objective function misfit curves of 3-D flexural modeling for 17 blocks profiles are shown in Figure 7.

It is notable that the  $T_e$  values obtained from 3-D flexural modeling are in excellent agreement with that of 2-D modeling along the NER except for the north-central part (Figure 5). In this part, the 2-D estimation suggests very high variability of  $T_e$  values from 4 to 22 km, whereas 3-D estimation suggests  $T_e$  values range between 5 and 15 km. However, lower  $T_e$  values in both models are in agreement, whereas higher values are overestimated in 2-D modeling case. The difference in higher values of  $T_e$  estimation between 2-D and 3-D modeling could be due to 1) incorrect dimensionality assumption in case of 2-D modeling, which predicts higher gravity anomalies, and thus leading to overestimation of  $T_e$ ; 2) less sensitivity of 3-D modeling to the change of  $T_e$  due to averaging over a region. The overestimation of  $T_e$  due to 2-D assumption typically occurs for circular features like seamounts as observed along the Louisville Ridge, Pacific Ocean [Lyons *et al.*, 2000]. Unlike the Louisville Ridge, north-central part of the NER is remarkably linear with a base topographical relief of 1.5-3 km from adjacent ocean floor, despite the FAA and residual geoid of north-central part are highly discontinuous with isolated belts of positive and negative anomalies. Hence, the highly variable  $T_e$  as suggested by 2-D modeling could be a result of variable gravitational response of lithosphere rather than assumption of wrong dimensionality. Also, if the 2-D assumption has a significant effect in  $T_e$ , the lower values as suggested by the 2-D modeling should have been systematically higher than that of 3-D modeling studies. Nevertheless, recent global  $T_e$  compilation using 3-D admittance analysis also suggests variable  $T_e$  values of 4-17 km for the NER [Kalins and Watts, 2012] providing strong support to our  $T_e$  estimates.



## 4.2 RMBA-Residual Topography Coherence Analysis

The traditional way of determining the  $Te$  is usually by comparing the observed and theoretical admittance function [Watts, 1978; Watts, 2001]. In this method, the theoretical admittance is calculated by loading of the elastic lithosphere from above (surface) and below (sub-surface or underplating). The best-fit model is obtained by changing three unknown parameters:  $Te$ , depth to the sub-surface load ( $z_d$ ) and sub-surface to surface loading ratio ( $f$ ). A strong plate with subsurface load and a weak plate with surface loading may give similar admittance results. Thus, different models with different  $Te$  may match with the observed admittance making the interpretations non-unique [Karner and Watts, 1983; Forsyth, 1985]. To overcome this uncertainty, an improved method based on the coherence analysis between RMBA and topography is considered to determine  $Te$  and subsurface loading [Forsyth, 1985; Luis and Neves, 2006]. The coherence is defined as

$$\gamma^2(\mathbf{k}) = \frac{C(\mathbf{k})C^*(\mathbf{k})}{E_g(\mathbf{k})E_t(\mathbf{k})} \quad (5)$$

Where  $C(k)$  is the cross-spectrum of bathymetry and gravity,  $E_g(k)$  and  $E_t(k)$  are power spectrum of the gravity and power spectrum of the topography, respectively. The theoretical coherence between RMBA and topography can be computed from

$$\gamma^2(\mathbf{k}) = \frac{\left(1 + \left(\frac{f}{\xi(\mathbf{k})}\right)^2 \varphi(\mathbf{k})\right)^2}{\left(1 + \left(\frac{f}{\xi(\mathbf{k})}\right)^2\right) \left(1 + f^2 \varphi(\mathbf{k})^2\right)} \quad (6)$$

$$\text{where, } \xi(\mathbf{k}) = \left[1 + \frac{Dk^4}{g(\rho_m - \rho_c)}\right]^{-1} \text{ and } \varphi(\mathbf{k}) = \left[1 + \frac{Dk^4}{g(\rho_c - \rho_w)}\right]^{-1}$$

We first computed coherence between RMBA and residual topography for the entire NER except the sediment covered northernmost part, for  $Te$  values ranging from 5 to 25 km assuming subsurface to surface loading ( $f$ ) of 0.5, and compared with theoretical coherence. The coherence versus wavelength plot (Figure 8a) shows a typical drop in coherence from 1 to 0.1 for wavelengths <100 km, indicating transition from compensated to uncompensated topography. At shorter wavelengths

(<100 km) the coherence values are not reliable due to noise in the data and hence are not used for the analysis. The breadth of transition of coherence from high to low at long-wavelengths clearly indicates that the NER is associated with variable compensation mechanisms (Figure 8a). The observed coherence could be explained by theoretical coherence curves for a wide range of  $Te$  values ( $Te = 5$  to 25 km), which clearly support the variable  $Te$  results of flexural modeling along the NER.

Further, coherence is computed for the 17 overlapping blocks on NER as used for the flexural modeling. Theoretical coherence was computed for a range of loading ratios and using  $Te$  values as obtained from 3-D flexural modeling for each of these blocks. The observed and theoretical coherence was compared for wavelengths >100 km to find out best-fit loading ratio. The best-fitting  $f$  values for each block are listed in Table 4. The observed and theoretical coherence curves for selected blocks for south, south-center, north-center and northern parts of the NER are presented in Figure 8b. On the whole the coherence analysis suggests the presence of subsurface loading beneath the entire NER with loading ratios between 0.2-0.6. The south and south-central and northern parts of the ridge are associated with a loading ratio of  $f = 0.2-0.35$ , whereas for the north-central part slightly higher loading ratios,  $f = 0.5-0.6$  are observed.

## **5. Geoid to topography ratio and apparent compensation depth below the NER**

The geoid to topography ratio ( $GTR$ ) is another important parameter commonly used for investigating the mode of isostatic compensation of volcanic loads on oceanic lithosphere as  $GTR$  is regarded as sensitive to the density distribution and depth of compensation of volcanic loads at the time of emplacement [Haxby and Turcotte, 1978; Sandwell and MacKenzie, 1989]. We computed  $GTR$  for 17 overlapping blocks along the NER. The computation is carried out using residual geoid and residual topography to avoid long-wavelength signals associated with density inhomogeneities caused by mantle convection processes. The residual topography data are filtered by removing spherical harmonic expansion of model topography up to degree and order 50 as in the case of residual geoid. The  $GTR$  is obtained from the slope of best fitting regression line through the correlation of residual geoid and residual topography. The estimated  $GTR$  is converted to the apparent depths of compensation ( $dc$ ) along the NER following the approach of Monnerneau and Cazenave [1988].

$GTR$  and corresponding apparent compensation depth ( $dc$ ) values for all 17 blocks are presented in Table 4 and the results are shown segment-wise in Figure 9. The  $GTR$  and  $dc$  values show considerable variation along the NER and closely follow the  $Te$  pattern estimated from the flexural

modeling (Table 4). This is additional evidence for the existence of variable isostatic compensation mechanisms beneath the entire NER. The low  $GTR$  ( $<1.2$ ) value for the southern part of the ridge indicates shallow depth of compensation (16-24 km) and crustal thickness of about 12-20 km. In contrast, the northern part of the NER is associated with very high  $GTR$  of about 2.7 indicating a very deep compensation of about 54 km.

## **6. Crustal Thickness Map of the NER**

The results of flexural modeling and coherence analysis (Figures 6a-d, 7 and 8a-b) indicate that the NER has variable compensation mechanisms with the presence of sub-crustal underplating material. However, neither of these results provides variation in crustal thickness beneath the NER. Therefore, we performed 3-D inversion of RMBA for computation of the Moho topography and crustal thickness beneath the entire NER. For 3-D inversion we used Parker–Oldenburg’s iterative algorithm implemented in MATLAB by *Oritze et al.* [2005]. We consider 12 km as an average depth to base of the crust and  $400 \text{ kg/m}^3$  as density at mantle-crust interface. A low pass cosine filter passing wavelengths  $>150$  and rejecting wavelengths  $<50$  is applied to RMBA before the downward continuation operation. This is required to prevent amplification of shorter wavelength anomalies during the process and to enhance the convergence in the iterative inversion scheme. The crustal thickness map is obtained by subtracting the bathymetry and sediment thickness from the Moho topography. For consistency, the bathymetry is filtered with the cosine filter that was used for the RMBA calculations. The computed crustal thickness map (Figure 10) suggests 12-22 km thick crust beneath the NER, which is thicker in comparison to the thickness of the crust (4-8 km) in the adjacent Central Indian and Wharton basins [*Krishna et al.*, 2001a].

## **7. Discussions**

### **7.1 Crustal structure beneath the NER**

A low  $Te$  ( $< 5$  km) value is typically considered as Airy compensation with very high crustal thickness, whereas moderate and high  $Te$  ( $>15$  km, and  $>25$  km) values correspond to flexural compensation [*Watts et al.*, 2006]. This model assumes that the volcanic loading is only from the top of the elastic plate. However, for most volcanic ridges, loading also occurs at the base of the elastic plate, and the subsurface load becomes a part of the crust. In such cases, the thickness of the crust can be high even with a high  $Te$  values. In the case of NER, inversion of RMBA suggests very high crustal thickness despite the highly variable  $Te$ . This could be due to the presence of subsurface loading below the ridge as obtained from the coherence analysis. An analysis of the

spatial variation of the crustal structure of NER and its relationship with  $T_e$  and subsurface loading is described below.

The crustal thickness map of the NER (Figure 10) shows >20 km thick crust beneath the southern and central parts of the NER. The results are comparable with the earlier reported results of excessive crustal thickness of central part of the NER using seismic refraction and OBS data [Grevemeyer *et al.*, 2001; Krishna *et al.*, 2001a]. Both studies suggested the presence of sub-crustal underplated rocks with velocities 7.3-7.8 km/s and a deep level of isostatic compensation with Moho boundary at a depth of about 25 km from the sea level. From Admittance analysis of gravity and bathymetry data, Grevemeyer *et al.* [2001] and Tiwari *et al.* [2003] also suggested deep flexure /Airy type compensation for the central part of the NER with crustal thickness of about 25-30 km.

In order to examine the crustal architecture of the NER, we compared the crustal model results derived in the present work with the crustal thickness results of the seismic studies. The Moho topography inferred from the inversion of RMBA and from the best fit  $T_e$  (18 km) is plotted along with the crustal model derived using OBS studies [Grevemeyer *et al.*, 2001] across the NER at 17°S (seis\_1) (Figures 10 and 11a). The flexural Moho is computed based on the assumption that crustal loading was on a normal oceanic crust of 6.5 km thick and basement depth prior to the loading was 5.5 km. Below the ridge topography, the flexural Moho closely follows the upper crustal boundary of the OBS-derived crustal layer, whereas the Moho topography derived from the RMBA inversion defines the base of the underplated rocks (Figure 11a). However, toward east of the NER, the prominent flexural up-lift as predicted by the flexural Moho is not observed in the OBS crustal boundary. Similarly, the RMBA derived Moho topography seems to have a slight off-set towards east compared to the OBS derived Moho boundary. These minor deviations do not seem to be unusual considering the assumptions made in the flexural modeling and RMBA inversion procedure. Nevertheless, it is, in general, considered that the elastic plate model predict the first order flexure caused by the surface load, whereas inverted Moho topography provides total crustal thickness including thickness of sub-crustal underplated material. However, the crustal thickness derived from RMBA inversion is depended on density contrast considered between the crust and mantle. We assumed a generally accepted value of 400 kg/m<sup>3</sup> as crust mantle density contrast to understand excess crustal thickness and density anomalies along the ridge. However, this assumption of density contrast, could be considered as an upper limit as high velocity underplated rocks are inferred from the OBS studies [Grevemeyer *et al.*, 2001] (Figure 11a). Consideration of lower density contrast between the underplated rocks and mantle may yield a relatively deeper Moho topography and

higher crustal thickness. Hence the present estimation could be considered as the lower limit of the Moho topography and crustal thickness variations.

The *GTR* of the central part of the NER (blocks B4 to B7) is about 1.3 m/km, which also suggests deep compensation of about 26 km. The ratio of subsurface to surface loading for the central part of the NER is about 0.2-0.35, which is much less than that of earlier estimations of about 1-2 [Tiwari *et al.*, 2003] and 0.7 [Grevemeyer *et al.*, 2001]. The difference could probably be explained by the differences in estimation methods adopted. Tiwari *et al.* [2003] estimation is based on admittance analysis keeping  $T_e$ , depth to the load and  $f$  as variables; this essentially means that the choice of  $f$  is subjective. Grevemeyer *et al.* [2001] estimated the volume based on the constraints from a single OBS observation and single isostatic compensation mechanism. Our estimation of the loading ratio is based on the RMBA-bathymetry coherence and essentially considers the surface and sub-surface loads as statistically independent processes and allows us to compute the variations in  $f$  with the  $T_e$ . Further, discussions about the variation in  $T_e$ ,  $f$  and the evolution of NER are included in section 7.2.

The crustal thickness of north-central part of the NER is about 12 km, which is 5-6 km greater than that of the normal oceanic crust. Further, we observe crustal thickness of more than 15 km beneath some isolated topographic highs (Figure 10). The *GTR* analysis also predicts depth of compensation of about 15-20 km for the north-central part of the ridge. Further we have compared the Moho topography derived from RMBA inversion and from best-fit  $T_e$  of 6 km with the OBS profile crossing the NER at 9.5°S (seis\_2) [Krishna *et al.*, 2001a] (Figures 10 and 11b). The OBS-derived crustal model demarcates the boundaries between oceanic layers 2A, 2B, 3A and 3B. However, the base of the layer 3B and mantle below the ridge topography that includes the underplated rocks in the crust were not identified in the OBS model (Figure 11b). Below the ridge topography, both flexural Moho and inverted Moho show deep flexure down to a depth of 19 - 20 km from sea surface. Away from the ridge, towards Central Indian and Wharton basins, the determined Moho topography generally matches with the base of OBS layer 3A (Figure 11b). The amplitude and wavelength of the predicted Moho flexure is comparable to that of the gravity forward model along this OBS profile [Krishna *et al.*, 2001a].

The crustal thickness for the northern part of NER is about 12-15 km and RMBA-topography analysis suggests  $f = 0.3-0.35$  with a high  $T_e$  value. Interestingly, the northernmost part of the NER possesses extremely high *GTR* of 2.7 corresponding to a depth of compensation of about 54 km, which is typically indicative of mid-plate thermal swells [Marks and Sandwell, 1991]. It should be noted that unlike gravity, geoid anomalies are more sensitive to compensations by large wavelength

lithospheric density anomalies and their consequent mantle flow [Hager, 1984]. The northern part of the NER is very close to the Andaman Subduction Zone and high geoid anomalies are observed along the subduction zones (Figure 3). Hence the high *GTR* associated with the northern part of NER may not be explained by simple isostatic compensation of the ridge topography.

In comparison to large crustal thickness derived beneath the NER, it is found that adjacent Wharton Basin, east of NER, has extremely low crustal thickness of 2-5 km. This observation is consistent with the low crustal thickness of the Wharton Basin derived using seismic [Singh *et al.*, 2010] and gravity studies [Radhakrishna *et al.*, 2010]. The lower crustal thickness beneath the Wharton Basin may have generated by the N-S oriented fracture zones and/or by the interaction of the Kerguelen hot spot with the Wharton spreading ridge segments. A detailed investigation is needed to understand the tectonic process that lead to extremely low crustal thickness in the Wharton Basin.

## **7.2 Variations of *Te* values along the NER and Geodynamic Implications**

2-D and 3-D flexural modeling and coherence analysis of RMBA data of the NER revealed extremely variable *Te* values ranging from 4 to 35 km along the entire length of the ridge. The flexural modeling was carried out with the consideration of only surface loading. However, an attempt has also been made to understand the effect of crustal underplating on *Te* estimation. As a test case, we examined the effect of subsurface loading with an average ratio ( $f = 0.3$ ) as obtained from the coherence analysis in flexural modeling. The difference in best fitting *Te* values is about 1-3 km, therefore we are of the view that subsurface load may not significantly influence the spatial variations in *Te* along the ridge. The pattern of the *Te* values is distinctly different from that of usual emplacement of volcanic constructs, where *Te* values are either uniform or follow some systematic trend. For example, the entire 85°E Ridge in northeastern Indian Ocean shows consistent *Te* values of 10-15 km [Sreejith *et al.*, 2011], whereas the Comorin Ridge shows both high (15 km) and low *Te* values (3 km) on its northern and southern parts, respectively [Sreejith *et al.*, 2008]. Similarly, the Hawaiian Ridge and the Chagos-Laccadive Ridge possess consistently high and low *Te* values and the Louisville Ridge has *Te* systematically increasing from SE to NW [Kalnins and Watts, 2012].

### *7.2.1 Emplacement of southern and northern parts of the NER*

Both flexural modeling and coherence analysis of the southern part of the NER reveal flexural compensation with *Te* values range from 10 to 14 km, suggesting an emplacement of volcanic rocks on a moderately rigid lithosphere. The present *Te* values are different from the earlier derived *Te* value of 22 km [Tiwari *et al.*, 2003], and it was indicated that this part of the ridge was emplaced in

an off-ridge setting. It should be noted that an “off-ridge” setting requires volcanic emplacement on a strong lithospheric plate that supports the enormous load created by the hot spot [Watts and ten Brink, 1989; Watts *et al.*, 2006]. Plate reconstruction models of eastern Indian Ocean suggest that south of 11°S the NER evolved along the 89°E FZ [Royer *et al.*, 1991]. This fracture zone kept growing along with the northward migration of the Wharton spreading ridge and acted as a structural and thermal boundary for the magma erupted by the Kerguelen hot spot. This clearly indicates that the eruption must have occurred along a plate that has been weakened by the 89°E FZ, therefore it is difficult to reconcile “off-ridge” scenario for the emplacement of southern part of the NER. The isostatic response of the ridge supports emplacement on an intermediately strong plate either on the flank of the Indian plate or on crust transferred from the Antarctic plate.

The northern part of the NER is also flexurally compensated, but with high  $T_e$  values greater than 25 km, suggesting the emplacement of this part of the ridge on a strong lithosphere. Plate reconstruction models suggest that the northern part of the NER was emplaced on a relatively old lithosphere during the Cretaceous Magnetic Quiet Period [Royer *et al.*, 1991; Krishna *et al.*, 2012]. Based on E-W lineations in the vertical gravity field corresponding to the extrusive features over the NER, Sager *et al.* [2010] suggested an emplacement of ridge near the spreading axis with successive ridge jumps towards the south. However, the idea of ridge jumps beneath the northern part of the NER remains elusive as the magnetic anomalies over the ridge are highly disturbed [Desa *et al.*, 2009].

### 7.2.2 Emplacement of central part of the NER

In contrast to both southern and northern parts of the NER, highly variable  $T_e$  (4-24 km) values are observed for the central part of the NER. Such high variability in  $T_e$  values along the hot spot track has not been previously reported, and this seems to be unique to the NER. New geochronology data along the NER [Pringle *et al.*, 2007, 2008] revealed linear north-south age progression from 77 to 43 Ma. Magnetic anomaly studies on either side of the NER suggest that the age of the oceanic crust west of the 86°E FZ increases from south to north, whereas the crustal age east of the 92°E FZ increases symmetrically in north and south directions about the Wharton fossil spreading ridge segments, which ceased at about 42 Ma [Krishna *et al.*, 1995; Krishna *et al.*, 2012]. The oceanic crust between the fracture zones includes complex age patterns with traces of fossil spreading ridge segments that ceased at 65 and 42 Ma [Royer *et al.*, 1991; Krishna *et al.*, 1995; Krishna and Gopala Rao, 2000]. This indicates that ridge segments within the corridor ceased spreading and jumped southward several times during the emplacement of the NER. The ridge jumps seem to have consistently occurred towards the hot spot and resulted in the capture of crustal segments that

initially belonged to the Antarctic plate and were subsequently added to the Indian plate [Krishna *et al.*, 2012]. This indicates that the parts of the NER emplaced in the Antarctic plate joined the Indian plate through southward ridge jumps. Evidence for successive ridge jumps is shown in the extrusive faulted structures observed in seismic reflection data and corresponding E-W trending vertical gravity gradients [Sager *et al.*, 2010].

An important implication of this complex interactions between the Kerguelen hot spot and the Wharton spreading ridge segments would impact on the mechanical properties of the oceanic lithosphere beneath the NER and hence the variation on  $T_e$  values. The formation of ridge segments on the Antarctic plate and the subsequent addition to the Indian plate indicates the emplacement of volcanic constructs of NER on a mechanically heterogeneous lithosphere of variable age and  $T_e$  values. This model also suggests that portions of the ridge that formed on Antarctic plate should have a reverse age pattern. However, the age data generated from sparse samples from NER do not indicate these expected age reversals. Lyons *et al.* [2000] observed that fossil spreading centers in the Pacific Ocean create discontinuity in  $T_e$  trends of the Louisville Ridge. However, in the case of NER a series of ridge jumps and complex age pattern exists and provides an excellent opportunity to examine the variations in  $T_e$  as a proxy of ridge jumps.

The variable random  $T_e$  values in the north-central part of the ridge may have occurred due to the emplacement of the ridge on lithosphere of complex age resulting from frequent southward ridge jumps. However, the south-central part of the NER shows a gradual increase in  $T_e$  values towards the south. Geochemical studies of rock samples from ODP Site 757, DSDP Site 214 and newly dredged samples from the south-central part of the ridge, suggest the interaction between the Kerguelen hot spot and the spreading center [Weis and Frey, 1991; Frey and Weis, 1995; Frey *et al.*, 2011]. The first ridge jump that occurred about 65 Ma brought the spreading center close to the hot spot leading to on-axis emplacement of the ridge. This hypothesis is supported by a low  $T_e$  values (<5 km) obtained for the south-central part of the NER from the present analysis. The gradual increase in  $T_e$  values towards the south up to 20 km near 18°S latitude probably indicates the occurrence of moderate ridge jumps capturing portions of NER originally formed on the Antarctic plate. The gap in  $T_e$  trend at about 21°S, which separates the south-central part from southern part of the ridge, may indicate the southern extent of this ridge jump. However, detailed magnetic surveys are needed to confirm the pattern of ridge jumps. Thus, the spatial variations in  $T_e$  suggest more frequent small ridge jumps for the north-central part and relatively moderate ridge jumps for south-central part of the NER.



Subsurface to surface loading ratio is another useful indicator for understanding the details of ridge-hot spot interactions. The loading ratio of north-central part of the NER is considerably higher (0.5-0.6) than that of the south-central part (0.2-0.3). In contrast, *Tiwari et al.* [2003] suggested high loading ratio for the south-central part considering the prolonged interaction of the Kerguelen hot spot with spreading ridge segments. However, the present tectonic model suggests that the north-central part of the ridge was emplaced during the intense ridge-hot spot interactions and frequent southward ridge jumps, therefore this part of the ridge can have more subsurface loading than the south-central part. The south-central part may have emplaced on the Indian lithospheric plate of intermediate strength. This lithosphere was originally formed on the Antarctic plate and transferred to Indian plate due to southward ridge jumps. The Kerguelen hot spot may have emplaced the volcanic materials over these transferred lithospheric pieces.

Another interesting observation is the role of the 89°E FZ during the evolution of the NER. The fracture zone that bounds the eastern edge of the southern part of the NER crosses the ridge at about 11°S, and thereafter borders the western edge of the ridge towards the north [*Krishna et al.*, 2012] (Figure 2). Interestingly, the NER-fracture zone junction separates the north-central part from the south-central part of the NER. This also forms a morphological boundary with north-central part having discontinuous eruption compared to continuous and prominent morphology of the south central part. It appears that the 89°E FZ has acted as a thermo-mechanical boundary for the extensive volcanism of the Kerguelen hot spot.

*Watts* [1978] proposed that  $T_e$  values of seamount chains depend on age and temperature gradient of the oceanic lithosphere at the time of loading and the effective elastic thickness roughly corresponds to 450±150°C isotherm of the cooling plate model. This suggests that the age of the oceanic crust beneath the central part of NER during the emplacement of the ridge is highly variable. However, such huge spatial variations in crustal age below the NER cannot be attributed to ridge jumps that can only cause age variations of about 5-10 myr. Similar to present observations, *Feighner et al.* [1994] found remarkable strength variations between south-western (flexure,  $T_e > 12$  km) and north-eastern (Airy,  $T_e < 6$  km) parts of the Galapagos islands, where the age difference of the lithosphere is only about 5-10 Myr. The NER and Galapagos islands are typical examples of volcanic eruptions during the complex interaction of the hot spot with the migrating mid-ocean ridge segments, which had also witnessed several ridge jumps. Therefore, we hypothesize that the ridge-hot spot interactions invoke thermal and mechanical weakening of the lithosphere, huge stress field generation and shear tractions at the base of the lithosphere, which may also result in lithospheric

strength variations. Thus, a simple plate cooling model defining  $T_e$  as the base of the isotherm may not be valid for such cases.

The tectonic model proposed for the evolution of the NER is compared with the existing models (Figure 12). The evolutionary model for the southern and northern part of the ridge agrees well with that of *Royer et al.* [1991] and *Krishna et al.* [1999], whereas for the central part a more complex model with interaction of spreading center with hot spot along with multiple ridge jumps beneath the NER is proposed. The north-central part must have emplaced on a crust of highly variable age produced by multiple southward ridge jumps, whereas the south-central part was emplaced on a crust of rather uniformly increasing age produced as a result of a moderate southward ridge jump.

## 8. Conclusions

Analyses of bathymetry, geoid and gravity data of the NER along 72 closely spaced transects and 17 overlapping blocks and results of 2-D and 3-D flexural modeling have provided new insights for understanding the isostatic compensation mechanisms, crustal structure and tectonic history of the ridge. The important observations are as follows:

1. 2-D and 3-D flexural modeling of the NER using bathymetry, residual geoid and gravity data reveal large spatial variation of  $T_e$  (4 to 35 km) along the entire length of NER. The southern (south of 22°S latitude) and northern (north of 2°N latitude) parts of the NER have  $T_e$  values of >10 and >23 km, respectively, whereas for the central part of the NER highly variable  $T_e$  values (4 to 22 km) are observed.

2. Variable isostatic compensation mechanisms that occurred in response to the volcanic loads along the NER are explained by the interaction of the Kerguelen hot spot with the Wharton spreading ridge segments. The southern part was emplaced on a lithosphere of intermediate strength possibly on the flank of the Indian plate or on a lithosphere transferred from the Antarctic plate, whereas the northern part was emplaced in an intraplate setting. The central part of the ridge evolved due to the occurrence of more frequent ridge jumps caused by the interaction of Kerguelen hot spot with rapid northward migration of the Wharton spreading ridge. Further, the spatial variations in  $T_e$  suggest more frequent small ridge jumps for the north-central part and relatively moderate ridge jumps for south-central part of the NER.

3. Inversion of RMBA data over the NER reveal the presence of a thick crust ranging from 15 to 19 km beneath the entire ridge. Further, coherence analysis of RMBA and residual topography reveals

that the ratio of sub-surface to surface load is about 0.2 to 0.6 for the NER. The  $T_e$  and crustal thickness results of the NER clearly show that the ridge possesses highly segmented compensation mechanisms with the presence of sub-crustal underplating or sub-surface loading.

### **Acknowledgments**

This work was carried out jointly by SAC, and CSIR-NIO as a part of MOP III–Marine Lithospheric Studies program. A.S. Kiran Kumar, Director-SAC, J.S. Parihar, DD-EPSA, Ajai GD-MPSG and A.S. Rajawat, Head-GSD from SAC have supported the collaborative studies. Figures were prepared using GMT software of *Wessel and Smith* [1997]. We thank Jon Bull for his comments and valuable suggestions on early version of the manuscript. This is NIO contribution No xxxx.

### **References**

- Bowin, C. (1973), Origin of the Ninetyeast Ridge from studies near the equator, *J. Geophys. Res.*, 78, 6029– 6043.
- Bull, J.M., and R.A. Scrutton (1992), Seismic reflection images of intraplate deformation, central Indian Ocean, and their tectonic significance, *J. Geol. Soc. Lon.*, 149, 955–966, doi: 10.1144/gsjgs.149.6.0955.
- Coffin, M., M.S. Pringle, R.A. Duncan, T.P. Gladchenko, M. Storey, R.D Mueller, and L.A. Gahagan (2002), Kerguelen hot spot magma output since 130 Ma, *J. Petrol.*, 43, 1121-1139, doi:10.1093/petrology/ 43.7.1121.
- Curry, J.R. (1994), Sediment volume and mass beneath the Bay of Bengal, *Earth Planet. Sci. Lett.*, 125, 371-383.
- Curry, J.R., F.J. Emmel, D.G. Moore, and W.R. Russel (1982), Structure, tectonics, and geological history of the northeastern Indian Ocean, in *The Ocean Basins and Margins, vol. 6, The Indian Ocean*, edited by A. E. Nairn and F. G. Stheli, pp. 399– 450, Plenum, New York.
- Desa, M., M.V. Ramana, and T. Ramprasad (2009), Evolution of the Late Cretaceous crust in the equatorial region of the Northern Indian Ocean and its implication in understanding the plate kinematics, *Geophys. J. Int.*, 177, 1265–1278.
- Detrick, R.S., and A.B. Watts (1979), An analysis of Isostasy in the world's oceans 3. Aseismic ridges, *J. Geophys. Res.*, 84, 3637-3653.
- Duncan, R.A. (1991), The age distribution of volcanism along aseismic ridges in the eastern Indian Ocean, *Proc. Ocean Drill. Program Sci. Results*, 121, 507– 517.
- Divins, D.L. (2009), NGDC Total Sediment Thickness of the World's Oceans and Marginal Seas. <http://www.ngdc.noaa.gov/mgg/sedthick/sedthick.html>

- Deplus, C., M. Diament, H. Hebert, G. Bertrand, S. Dominguez, J. Dubois, J. Malod, P. Patriat, B. Pontoise, and J.J. Sibilla (1998), Direct evidence of active deformation in the eastern Indian oceanic plate, *Geology*, 26, 131-134.
- Frey, F.A., J.S. Jr Dickey, G. Thompson, and W.B. Bryan (1977), Eastern Indian Ocean DSDP Sites: correlations between petrography, geochemistry, and tectonic setting: in *A synthesis of deep sea drilling in the Indian Ocean*, edited by J.R. Heirtzler, et al., pp 189-257, U.S. Government printing office, Washington, D.C.
- Frey, F.A., and D. Weis (1995), Temporal evolution of the Kerguelen plume; Geochemical evidence from approximately 38 to 82 Ma lavas forming the Ninetyeast Ridge, *Contrib. Mineral. Petrol.*, 121, 12-28.
- Frey, F.A., M. Pringle, P. Meleney, S. Huang, and A. Piotrowski (2011), Diverse mantle sources for Ninetyeast Ridge magmatism: Geochemical constraints from basaltic glasses, *Earth Planet. Sci. Let.*, 303, 215-224, doi:10.1016/j.epsl.2010.12.051
- Feighner, M.A., and M.A. Richards (1994), Lithospheric structure and compensation mechanisms of the Galapagos Archipelago, *J. Geophys. Res.*, 99, 6711-672.
- Forsyth, D.W. (1985), Subsurface loading and estimates of the flexural rigidity of continental lithosphere, *J. Geophys. Res.*, 90, 12,623 - 12,632, 1985.
- Gopala Rao, D., K.S. Krishna, and D. Sar (1997), Crustal evolution and sedimentation history of the Bay of Bengal since the Cretaceous, *J. Geophys. Res.*, 102, 17,747-17,768, doi:10.1029/96JB01339.
- Grevemeyer, I., and E.R. Flueh (2000), Crustal Underplating and its implications for subsidence and state of isostasy along the Ninetyeast Ridge hot spot trail, *Geophys. J. Int.*, 142, 643-649.
- Grevemeyer, I., E.R. Flueh, C. Reichert, J. Bialas, D. Klaschen and C. Kopp (2001), Crustal architecture and deep structure of the Ninetyeast Ridge hot spot trail from active-source ocean bottom seismology, *Geophys. J. Int.*, 144, 414-431.
- Hager, B.H. (1984), Subducted slabs and the Geoid: Constraints on mantle rheology and flow, *J. Geophys. Res.*, 89, 6003-6015.
- Haxby W.F., and D.L. Turcotte (1978), On isostatic geoid anomalies, *J. Geophys. Res.*, 83, 5473-5478.
- Kalnins L.M., and A.B. Watts (2012), A global grid of lithospheric strength (*Te*) in the world's Oceans, *Geophys. Res. Let.*, (Submitted)
- Karner, G.D., and A.B. Watts (1983), Gravity anomalies and flexure of lithosphere at mountain ranges, *J. Geophys. Res.*, 88, 10449-10477.
- Krishna, K.S., D. Gopala Rao, M.V. Ramana, V. Subrahmanyam, K.V.L.N.S. Sarma, A.I. Pilipenko, V.S. Shcherbakov, and I.V. Radhakrishna Murthy (1995), Tectonic model for the evolution of oceanic crust in the northeastern Indian Ocean from the Late Cretaceous to the early Tertiary, *J. Geophys. Res.*, 100, 20,011- 20,024, doi:10.1029/94JB02464.

- Krishna, K.S., D. Gopala Rao, L.V. Subba Raju, A.K. Chaubey, V.S. Shcherbakov, A.I. Pilipenko, and I.V. Radhakrishna Murthy (1999), Paleocene on-axis hot spot volcanism along the Ninetyeast Ridge: An interaction between the Kerguelen hot spot and the Wharton spreading center, *Proc. Indian Acad. Sci. (Earth Planet. Sci.)*, 108, 255-267.
- Krishna, K. S., and D. Gopala Rao (2000), Abandoned Paleocene spreading center in the northeastern Indian Ocean: Evidence from magnetic and seismic reflection data, *Mar. Geol.*, 162, 215–224, doi:10.1016/S0025-3227(99)00085-7.
- Krishna, K.S., Y.P. Neprochnov, D. Gopala Rao, and B.N. Grinko (2001a), Crustal structure and tectonics of the Ninetyeast Ridge from seismic and gravity studies, *Tectonics*, 20, 416-433, doi:10.1029/2001TC900004.
- Krishna, K.S., J.M. Bull, and R.A. Scrutton (2001b), Evidence for multiphase folding of the central Indian Ocean lithosphere, *Geology*, 29, 715-718, doi:10.1130/0091-7613(2001)029<0715:EFMFOT>2.0.CO;2.
- Krishna K.S., J.M. Bull, and R.A. Scrutton (2009), Early (pre-8 Ma) fault activity and temporal strain accumulation in the central Indian Ocean, *Geology*, 37, 227-230.
- Krishna, K.S., Abraham, H., Sager, W.W., Gopala Rao, and D., Levchenko. (2012), Tectonics of the Ninetyeast Ridge derived from the spreading records of the contiguous oceanic basins and age constraints of the ridge, *J. Geophys. Res.* 117, B04101, doi:10.1029/2011JB008805.
- Levchenko, O.V., V.Ye., Milanovskiy, and A.A., Popov (1993), A sediment thickness map and tectonics of the distal Bengal Fan, *Oceanology*, 33, 2, 232-238.
- Lyons, S. N., D. T., Sandwell, W. H. F., and Smith (2000), Three-dimensional estimation of elastic thickness under the Louisville ridge, *J. Geophys. Res.*, 105, 13,239-13,252.
- Luis, F.F. and M.C. Neves (2006), The isostatic compensation of the Azores Plateau: A 3D admittance and coherence analysis, *J. Geothermal Vulc. Res.* 156, 10-22.
- Marks K.M. (1996), Resolution of the Scripps/NOAA marine gravity field from satellite altimetry, *Geophys. Res. Lett.*, 23, 2069-2072.
- Michael, L., and K.S. Krishna (2011), Dating of the 85°E Ridge (northeastern Indian Ocean) using marine magnetic anomalies, *Curr. Sci.*, 100, 1314-1322.
- Mueller, R.D., W.R. Roest, J.-Y. Royer, L.M. Gahagan, and J.G., Sclater (1997), Digital isochrones of the world's ocean floor, *J. Geophys. Res.*, 102, 3211-3214.
- Ortiz., D.G., and B.N.P. Agarwal (2005), 3DINVER.M: a MATLAB program to invert the gravity anomaly over a 3D horizontal density interface by Parker–Oldenburg's algorithm, *Computers & Geosciences*, 31, 513-520
- Monnereau, M., and A. Cazenave (1988), Variation of the apparent compensation depth of hot spot swells with age of plate, *Earth Planet. Sci. Lett.*, 91, 179-197.
- Parker, R.L. (1972), The rapid calculation of potential anomalies, *Geophys. J. R. Astr. Soc.*, 31, 447-455.

- Peirce, J.W. (1978), The Northward Motion of India since the Late Cretaceous, *Royal Astro. Soc. Geophys. J.*, 52, 277-311.
- Pringle, M.S., F.A. Frey, E.M. Mervine, and W.W. Sager (2007), New Ar/Ar ages from the Ninetyeast Ridge, Indian Ocean: Beginning of a robust Indo-Atlantic hot spot reference frame, *EOS, Trans. AGU*, 88 (52), Fall Mtg. Supplement, abstract U13A-0871.
- Pringle, M.S., F.A. Frey, and E.M. Mervine (2008), A simple linear age progression for the Ninetyeast Ridge, Indian Ocean: New constraints on Indian plate motion and hot spot dynamics, *EOS, Trans. AGU*, 89 (53) Fall Mtg. Suppl., abstract T54B-03.
- Radhakrishna, M., C. Subrahmanyam and T. Damodharan (2010), Thin crust below Bay of Bengal inferred from 3-D gravity interpretation, *Tectonophysics*, 493, 93-105.
- Rapp, R.H. (1998), Comparison of altimetry derived and ship gravity anomalies in the vicinity of the Gulf of California, *Mar. Geod.*, 21, 245–259.
- Royer, J.-Y., and D.T. Sandwell (1989), Evolution of the eastern Indian Ocean since the late Cretaceous: Constraints from Geosat altimetry, *J. Geophys. Res.*, 94, 13,755–13,782, doi:10.1029/JB094iB10p13755.
- Royer, J.-Y., J.W. Peirce, and J.K. Weissel (1991), Tectonic constraints on the hot spot formation of Ninetyeast Ridge, *Proc. ODP, Sci. Res.*, 121, 763-776.
- Sager, W.W., C.F. Paul, K.S. Krishna, M. Pringle, A.E. Eisin, F.A. Frey, D. Gopala Rao, and O. Levchenko (2010), Large fault fabric of the Ninetyeast Ridge implies near spreading ridge formation, *Geophys. Res. Lett.*, 37, L17304, doi:10.1029/2010GL044347.
- Sager, W.W., J.M. Bull, and K.S. Krishna (2013), Active Faulting in the Ninetyeast Ridge and its relation to deformation of the Indo-Australian Plate, *J. Geophys. Res.*, 118, doi:10.1002/jgrb.50319.
- Sandwell, D.T., and W.H.F. Smith (2009), Global marine gravity from retracked Geosat and ERS-1 altimetry: Ridge segmentation versus spreading rate, *J. Geophys. Res.*, 114, B01411, doi:10.1029/2008JB006008.
- Sandwell, D.T., and K.R. MacKenzie (1989), Geoid height versus topography for oceanic plateaus and swells, *J. Geophys. Res.* 94, 7403–7418.
- Sclater, J.G., and R.L. Fisher (1974), Evolution of the east central Indian Ocean, with emphasis on the tectonic setting of the Ninetyeast Ridge, *Geol. Soc. Am. Bull.*, 85, 683-702.
- Singh, S.C., H. Carton, A.S. Chauhan, S. Androvandi, A. Davaille, J. Dymant, M. Cannat, and N.D. Hananto (2010), Extremely thin crust in the Indian Ocean possibly resulting from Plume-Ridge Interaction, *Geophys. J. Int.*, doi: 10.1111/j.1365-246X.2010.04823.x
- Smith, W.H.F., and D.T. Sandwell (1997), Global seafloor topography from Satellite altimetry and ship depth soundings, *Science*, 277, 1956–1962.
- Smith, W.H.F., H., Staudigel, A.B. Watts, and M.S. Pringle (1989), The Magellan seamounts: Early Cretaceous record of the South Pacific isotopic and thermal anomaly, *J. Geophys. Res.*, 94: 10501-10523.

- Sreejith, K.M., K.S. Krishna, A.R. Bansal (2008), Structure and isostatic compensation of the Comorin Ridge, North-Central Indian Ocean, *Geophys. J. Int.*, 175, 729-741
- Sreejith, K.M., M. Radhakrishna, K.S. Krishna, and T.J. Majumdar (2011), Development of the negative gravity anomaly of the 85°E Ridge, northeastern Indian Ocean – a process oriented modeling approach, *J. Earth. Syst. Sci.*, 120, 605-615.
- Sreejith, K.M., S. Rajesh, T.J. Majumdar, G. Srinivasa Rao, M. Radhakrishna, K.S. Krishna, and A.S., Rajawat (2013), High-resolution residual geoid and gravity anomaly data of the northern Indian Ocean - an input to geological understanding, *J. Asian. Earth. Sci.*, 62, 616-626.
- Stein, C. A., and S. Stein (1992), A model for the global variation in oceanic depth and heat flow with lithospheric age, *Nature*, 359, 123–129.
- Tiwari, V.M., M. Diament, and S.C. Singh (2003), Analysis of satellite gravity and bathymetry data over Ninety-East Ridge: variation in the compensation mechanism and implication for emplacement process, *J. Geophys. Res.*, 108(B2), 2109, doi:10.1029/2000JB000047.
- Watts, A.B. (1978), An analysis of isostasy in the world's oceans: Hawaiian-Emperor Seamount Chain, *J. Geophys. Res.*, 83, 5989-6004.
- Watts, A.B., and U.S., ten Brink (1989), Crustal structure, flexure and subsidence history of the Hawaiian Islands, *J. Geophys. Res.*, 94, 10,473– 10,500.
- Watts, A.B. (2001), *Isostasy and flexure of the lithosphere*, Cambridge University Press, UK.
- Watts, A.B., D.T. Sandwell, W.H.F. Smith, and P. Wessel (2006), Global gravity, bathymetry, and the distribution of submarine volcanism through space and time, *J. Geophys. Res.*, 111, B08408, doi: 10.1029/2005JB004083.
- Weis, D., F.A. Frey, A. Saunders, I. Gibson (1991), Leg 121 Scientific Shipboard Party, Ninetyeast Ridge (Indian Ocean): A 5000 km Record of a Dupal Mantle Plume, *Geology*, 19, 99-102.

## Figure Captions:

**Figure 1:** Satellite derived bathymetry map [Smith and Sandwell, 1997] of the northeastern Indian Ocean with 4000 m depth contour (left panel). Ship-borne and satellite gravity profiles investigated in the present work are shown with dashed black and white solid lines, respectively. Ship-borne profiles are projected orthogonal to the strike of the NER and shown with black solid lines. The positions of 550 km  $\times$  550 km overlapping blocks (B1-B17) are shown separately on the lower right panel. The block names are written along the southern side of each block. Blocks B1 and B17 are shaded. The regional bathymetry map of the Indian Ocean along with locations of major aseismic ridges, plateaus and plate boundaries are presented in the upper right panel. BR = Broken Ridge, CR = Carlsberg Ridge, CIR = Central Indian Ridge, SWIR = Southwest Indian Ridge, SEIR = Southeast Indian Ridge.

**Figure 2:** Satellite derived free-air gravity anomaly map [Sandwell and Smith, 2009] of the northeastern Indian Ocean. Magnetic lineations (thin line), fossil spreading centers (thick dashed lines) and fracture zones (white dashed line) of the region adjacent to the NER [Krishna *et al.*, 2012] are placed over the gravity map. DSDP and ODP sites (solid circles) are shown with new geochronology dates.

**Figure 3:** Residual geoid anomaly map of the NER and surrounding areas.

**Figure 4:** Residual Mantle Bouguer Anomaly (RMBA) map of the NER.

**Figure 5:** Variations of  $T_e$  values derived from 2-D and 3-D flexural modeling along the NER from 28°S to 8°N. The error bars represent lower and upper bounds of  $T_e$  estimates. Values are listed in Tables 2 and 3. Bathymetry, Moho depths derived from the inversion of RMBA data, gravity and residual geoid on a longitudinal transect along the NER are also shown. Radiometric ages derived from the rock samples of DSDP and ODP drill sites along the NER [Pringle *et al.*, 2008] show 118 km/Myr rate of accretion.

**Figure 6a:** Flexural modeling along selected profiles from the southern part of the NER. Observed and predicted gravity (black) and geoid (gray) curves for the best fit  $T_e$  values are shown. The objective function misfit curve for the profiles is shown in the upper panel. Best fit  $T_e$  with errors for the 72 profiles are listed in Table 2.

**Figure 6b:** Flexural modeling along selected profiles from the south-central part of the Ninetyeast Ridge. Figure format is same as Figure 6a.



**Figure 6c:** Flexural modeling along selected profiles from the north-central part of the Ninetyeast Ridge. Figure format is same as Figure 6a.

**Figure 6d:** Flexural modeling along selected profiles from the northern part of the Ninetyeast Ridge. Figure format is same as Figure 6a.

**Figure 7:** Objective function misfit for 3-D flexural modeling of gravity (black) and geoid (gray) along blocks B1-B17. The best fit  $T_e$  with error bounds are listed in Table 3.

**Figure 8a:** Observed coherence between RMBA data and residual topography of the NER (28°S to equator) with theoretical coherence for  $T_e$  values 5 to 25 assuming  $f = 0.5$ .

**Figure 8b:** Observed coherence between RMBA data and residual topography of the NER from selected blocks (having close  $T_e$  values) from the southern, south-central, north-central and northern parts of the NER with theoretical coherence for  $f=0.1$  to  $0.5$ .

**Figure 9:** Geoid to topography ratio ( $GTR$ ) and apparent compensation depth ( $dc$ ) for 4 ridge segments along the NER. The values of  $GTR$  and  $dc$  for blocks B1-B17 are listed separately in Table 4.

**Figure 10:** Moho topography and crustal thickness maps of the NER obtained from the inversion of RMBA data (Figure 4). Location of OBS profiles *seis\_1* (17°S) and *seis\_2* (9.5° S) are shown on the Moho topography map.

**Figure 11a:** Comparison of Moho topography derived from the inversion of RMBA data and flexural modeling study with the OBS-derived crustal model [*Grevymeyer et al., 2001*] along *seis\_1* (approximately along 17°S latitude).

**Figure 11b:** Comparison of Moho topography derived from the inversion of RMBA data and flexural modeling study with the OBS-derived crustal model [*Krishna et al., 2001a*] along *seis\_2* (approximately along 9.5°S latitude).

**Figure 12:** Evolutionary model proposed for the accretion of the NER, showing the Kerguelen hot spot location with reference to the Wharton spreading centers. The present model is compared with the existing models [*Royer et al., 1991, Krishna et al., 1999; Tiwari et al., 2003*].

#### **List of Tables:**

**Table 1:** Model parameters used for the flexural computations

**Table 2:**  $T_e$  values along the NER (south to north) obtained by 2-D flexural modeling of gravity-topography and geoid-topography data sets

**Table 3:**  $T_e$  values along the NER (south to north) obtained by 3-D flexural modeling using gravity-topography and geoid-topography data sets.

**Table 4:** Results of coherence analysis and geoid to topography ratio analysis of 17 overlapping blocks (B1-B17). The best fit  $T_e$  is the average of  $T_e$  estimations using gravity-topography and geoid topography analysis. For each block, the ratio of sub-surface to surface loading ratio ( $f$ ),  $GTR$  and apparent compensation depths ( $dc$ ) are listed.

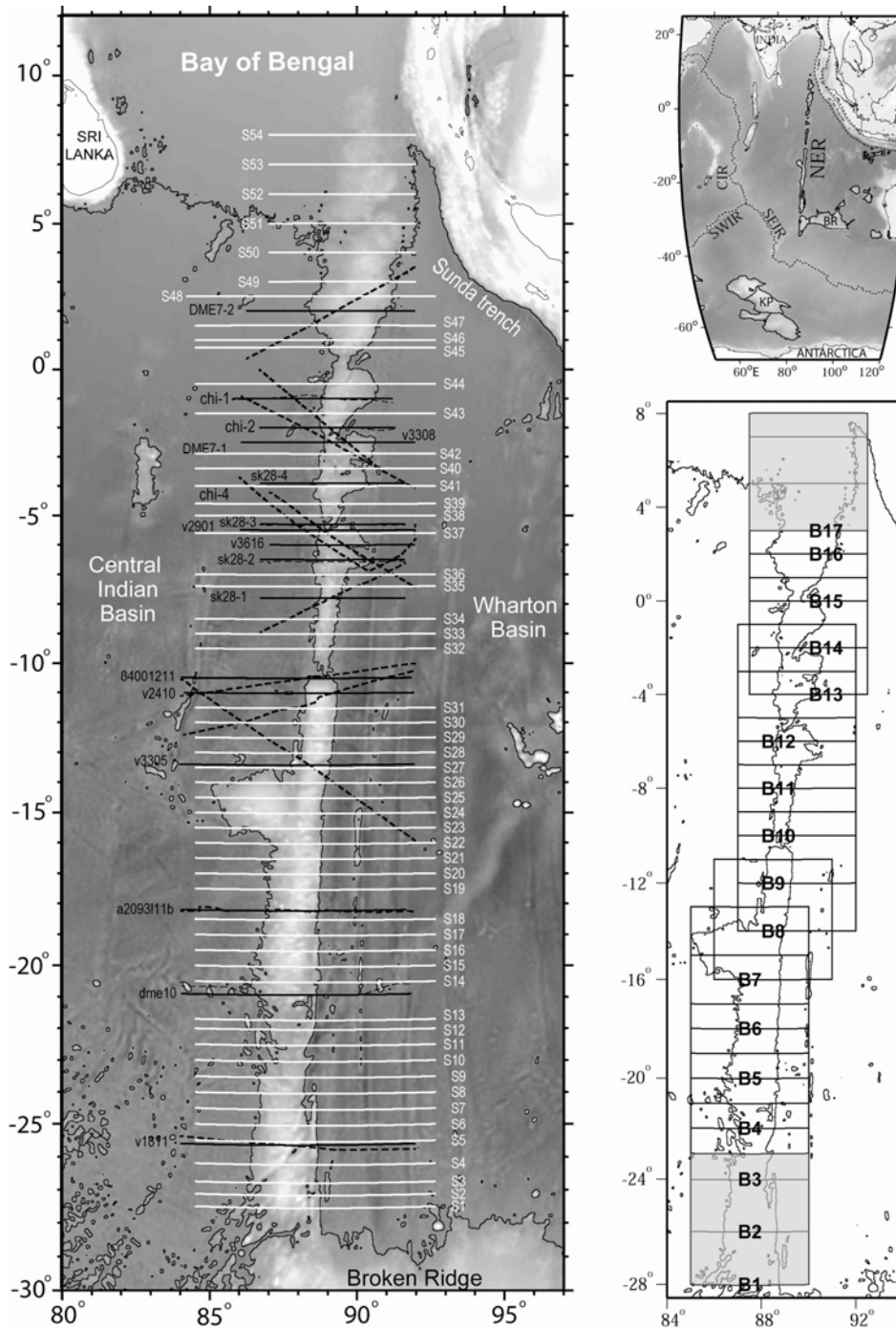


**Figure 1:** Satellite derived bathymetry map [Smith and Sandwell, 1997] of the northeastern Indian Ocean with 4000 m depth contour (left panel). Ship-borne and satellite gravity profiles investigated in the present work are shown with dashed black and white solid lines, respectively. Ship-borne profiles are projected orthogonal to the strike of the NER and shown with black solid lines. The positions of 550 km × 550 km overlapping blocks (B1-B17) are shown separately on the lower right panel. The block names are written along the southern side of each block. Blocks B1 and B17 are shaded. The regional bathymetry map of the Indian Ocean along with locations of major aseismic ridges, plateaus and plate boundaries are presented in the upper right panel. BR = Broken Ridge, CR = Carlsberg Ridge, CIR = Central Indian Ridge, SWIR = Southwest Indian Ridge, SEIR = Southeast Indian Ridge.

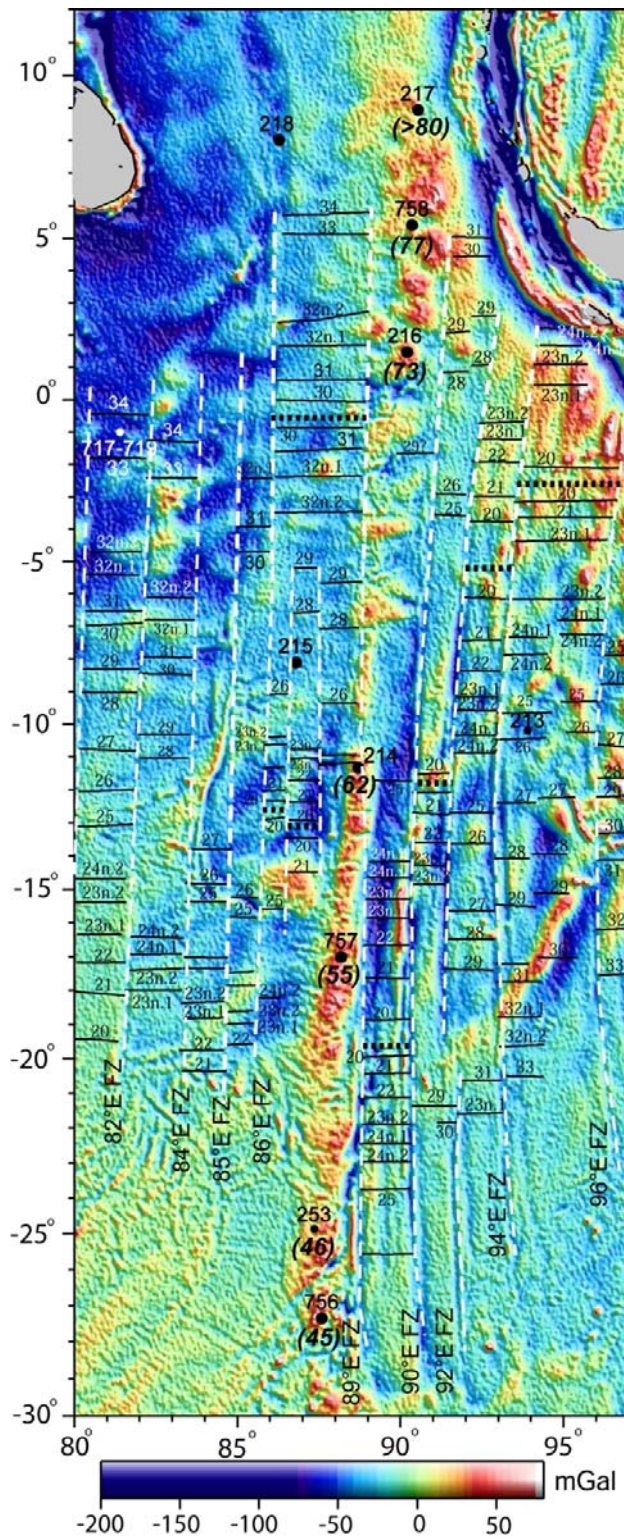


**Figure 2:** Satellite derived free-air gravity anomaly map [Sandwell and Smith, 2009] of the northeastern Indian Ocean. Magnetic lineations (thin line), fossil spreading centers (thick dashed lines) and fracture zones (white dashed line) of the region adjacent to the NER [Krishna et al., 2012] are placed over the gravity map. DSDP and ODP sites (solid circles) are shown with new geochronology dates.



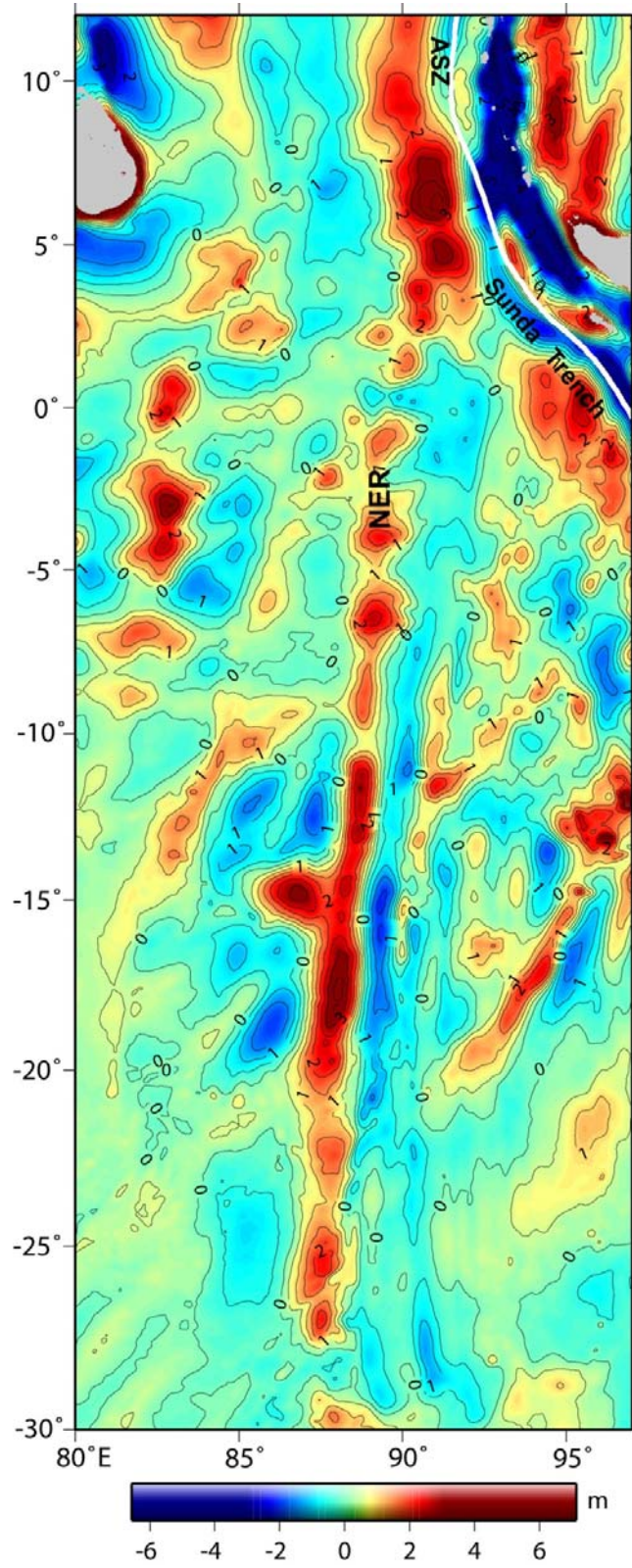


**Figure 3:** Residual geoid anomaly map of the NER and surrounding areas.

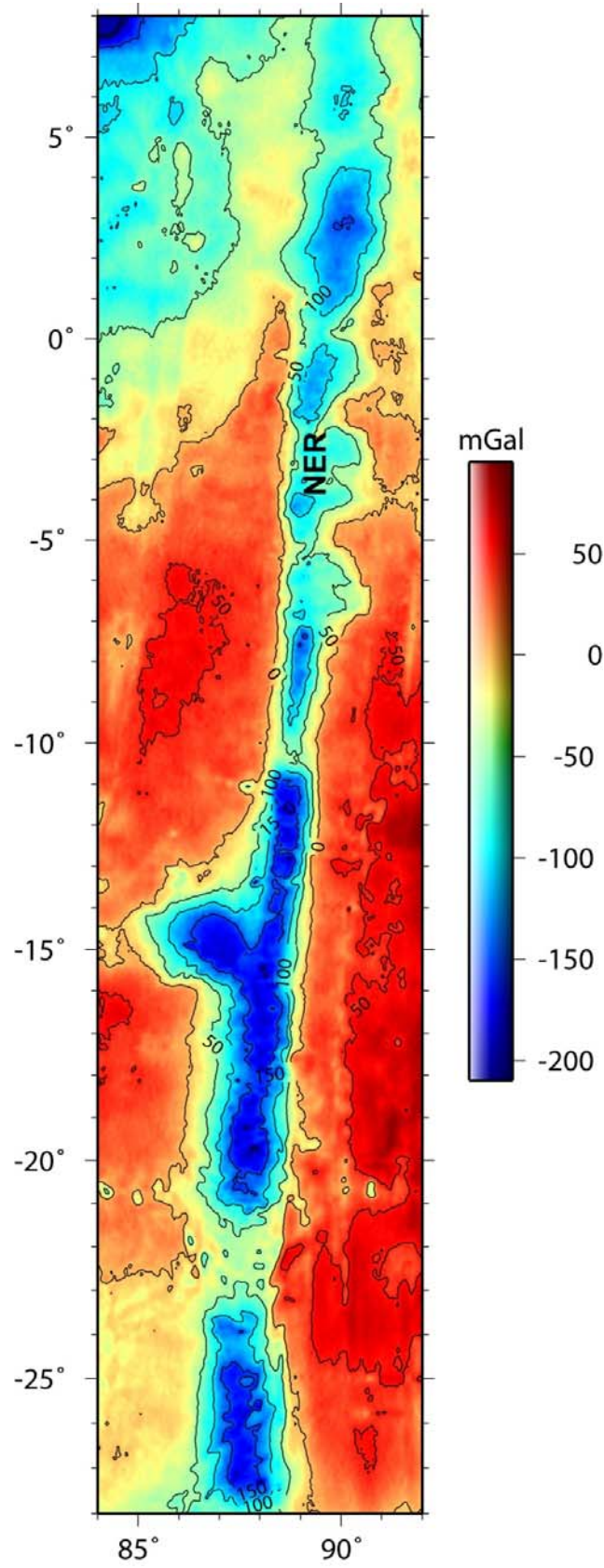


**Figure 4:** Residual Mantle Bouguer Anomaly (RMBA) map of the NER.

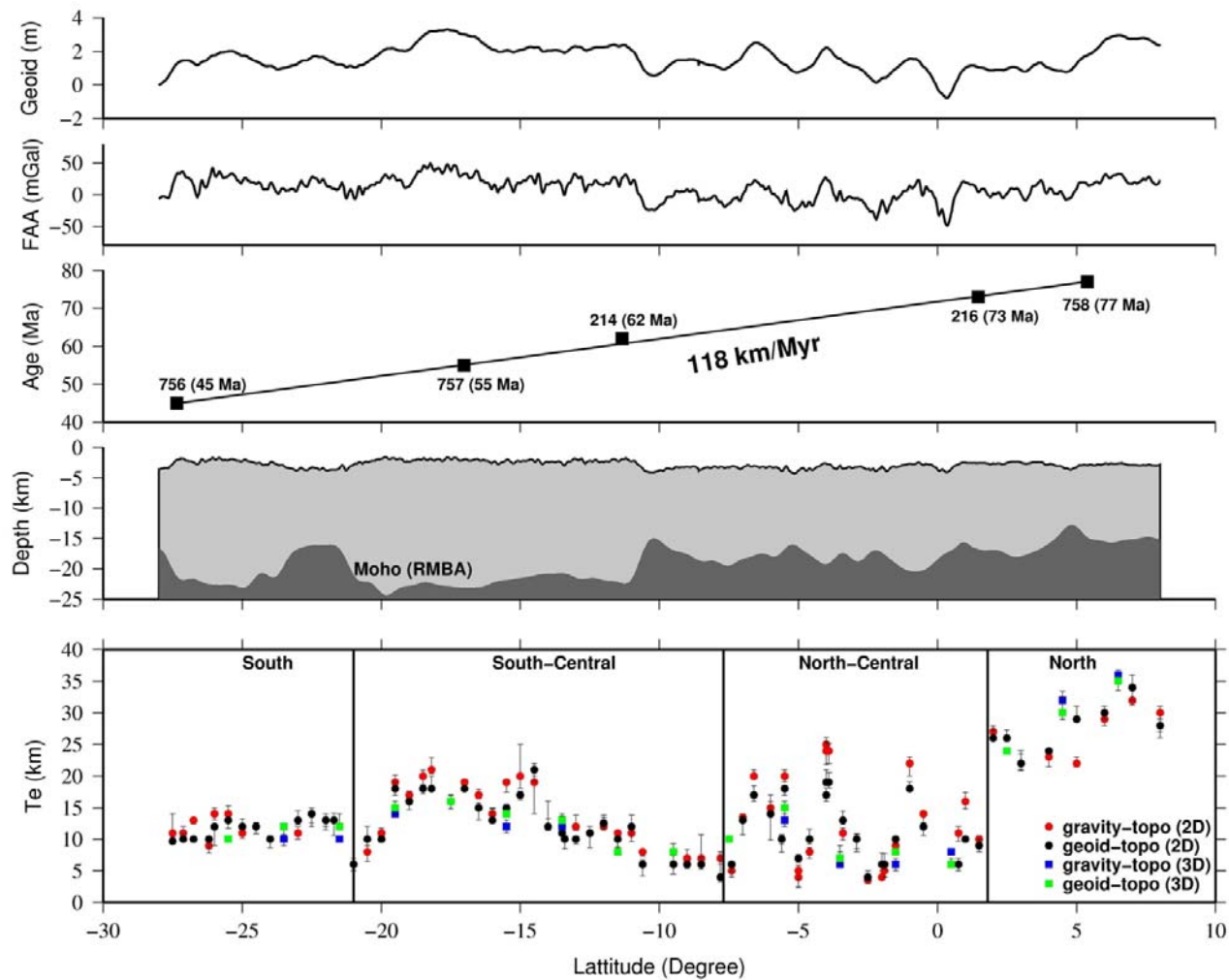


**Figure 5:** Variations of  $T_e$  values derived from 2-D and 3-D flexural modeling along the NER from 28°S to 8°N. The error bars represent lower and upper bounds of  $T_e$  estimates. Values are listed in Tables 2 and 3. Bathymetry, Moho depths derived from the inversion of RMBA data, gravity and residual geoid on a longitudinal transect along the NER are also shown. Radiometric ages derived from the rock samples of DSDP and ODP drill sites along the NER [Pringle *et al.*, 2008] show 118 km/Myr rate of accretion.

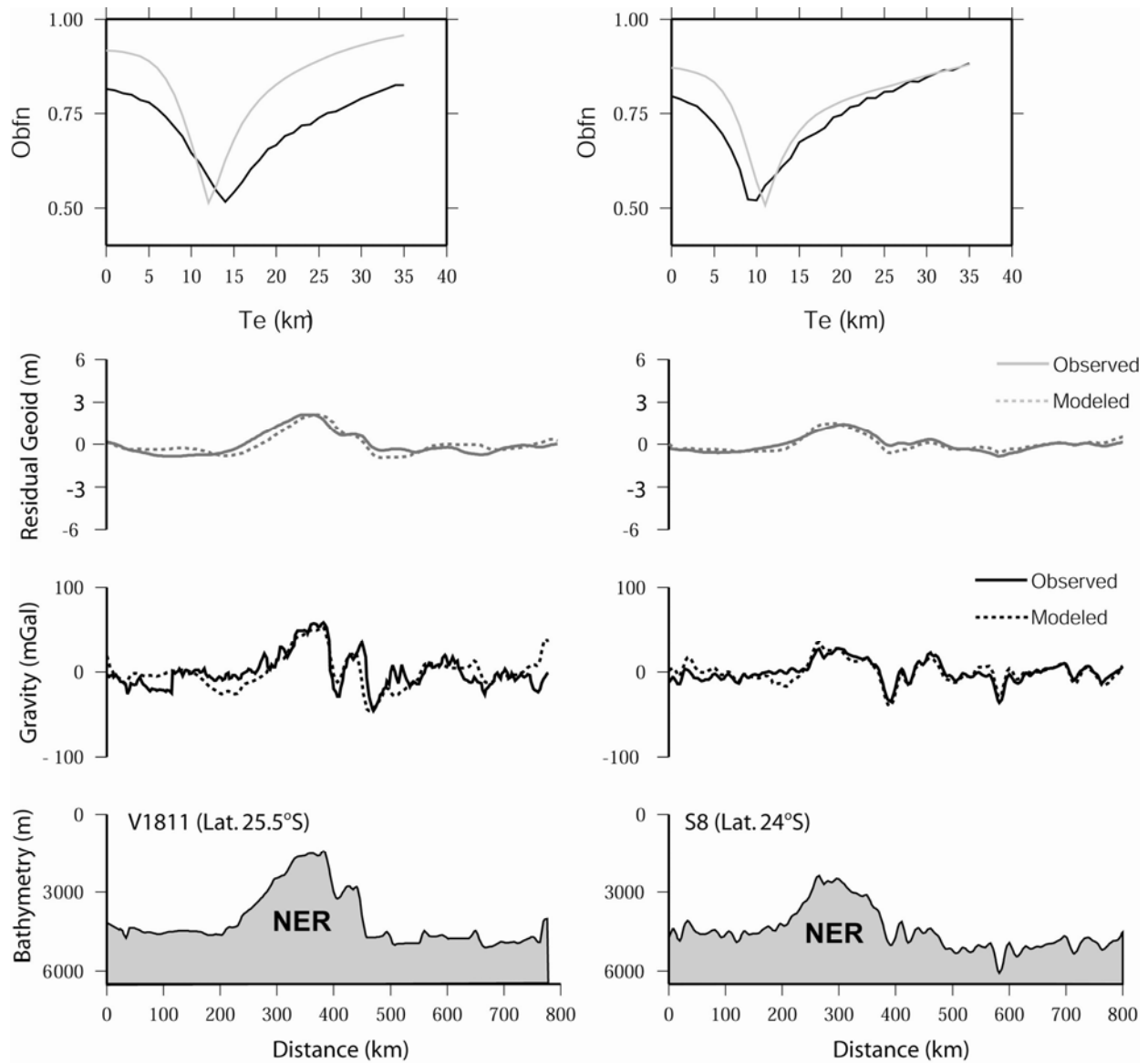


**Figure 6a:** Flexural modeling along selected profiles from the southern part of the NER. Observed and predicted gravity (black) and geoid (gray) curves for the best fit  $T_e$  values are shown. The objective function misfit curve for the profiles is shown in the upper panel. Best fit  $T_e$  with errors for the 72 profiles are listed in Table 2.



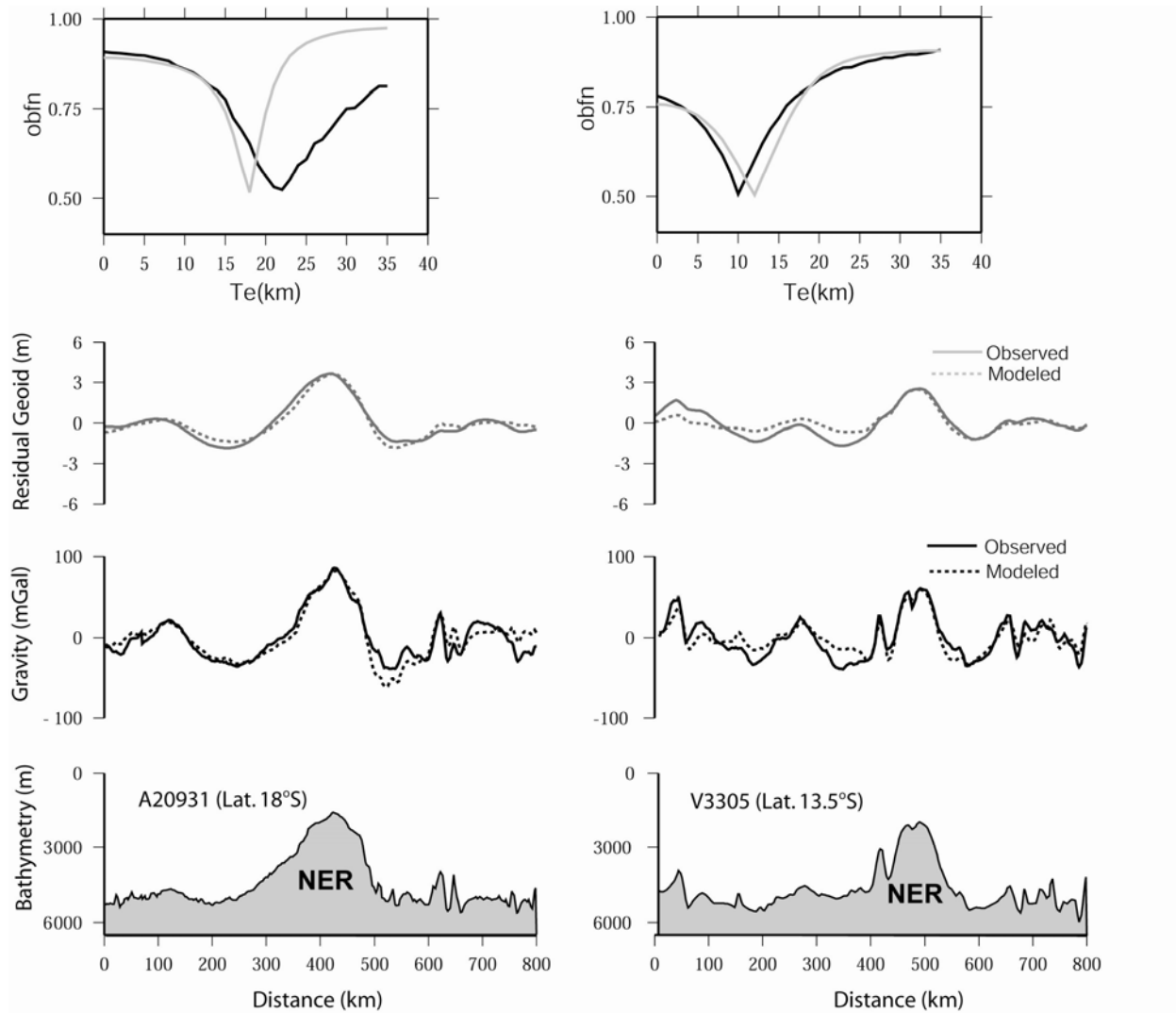


**Figure 6b:** Flexural modeling along selected profiles from the south-central part of the Ninetyeast Ridge. Figure format is same as Figure 6a.

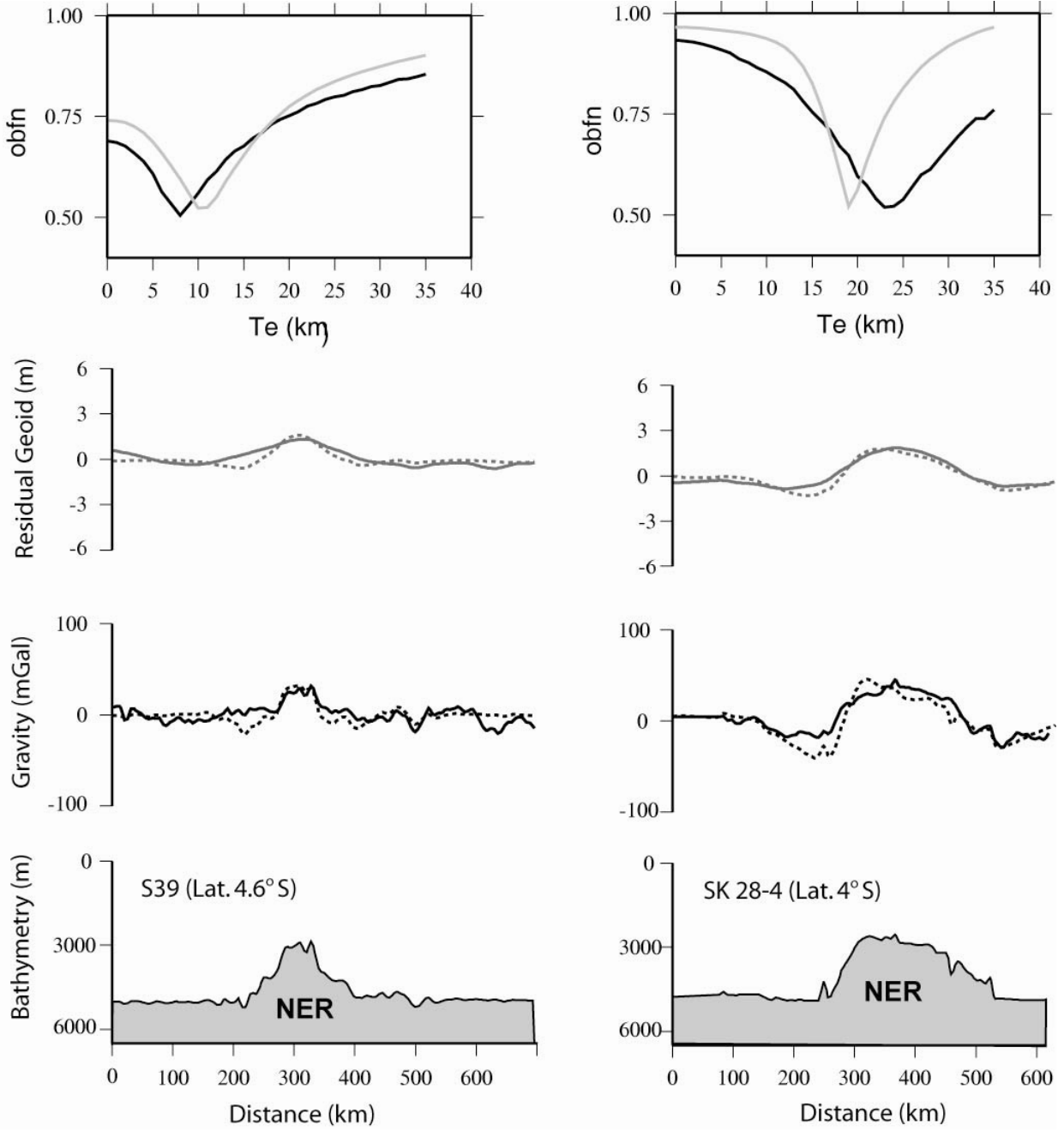


**Figure 6c:** Flexural modeling along selected profiles from the north-central part of the Ninetyeast Ridge. Figure format is same as Figure 6a.

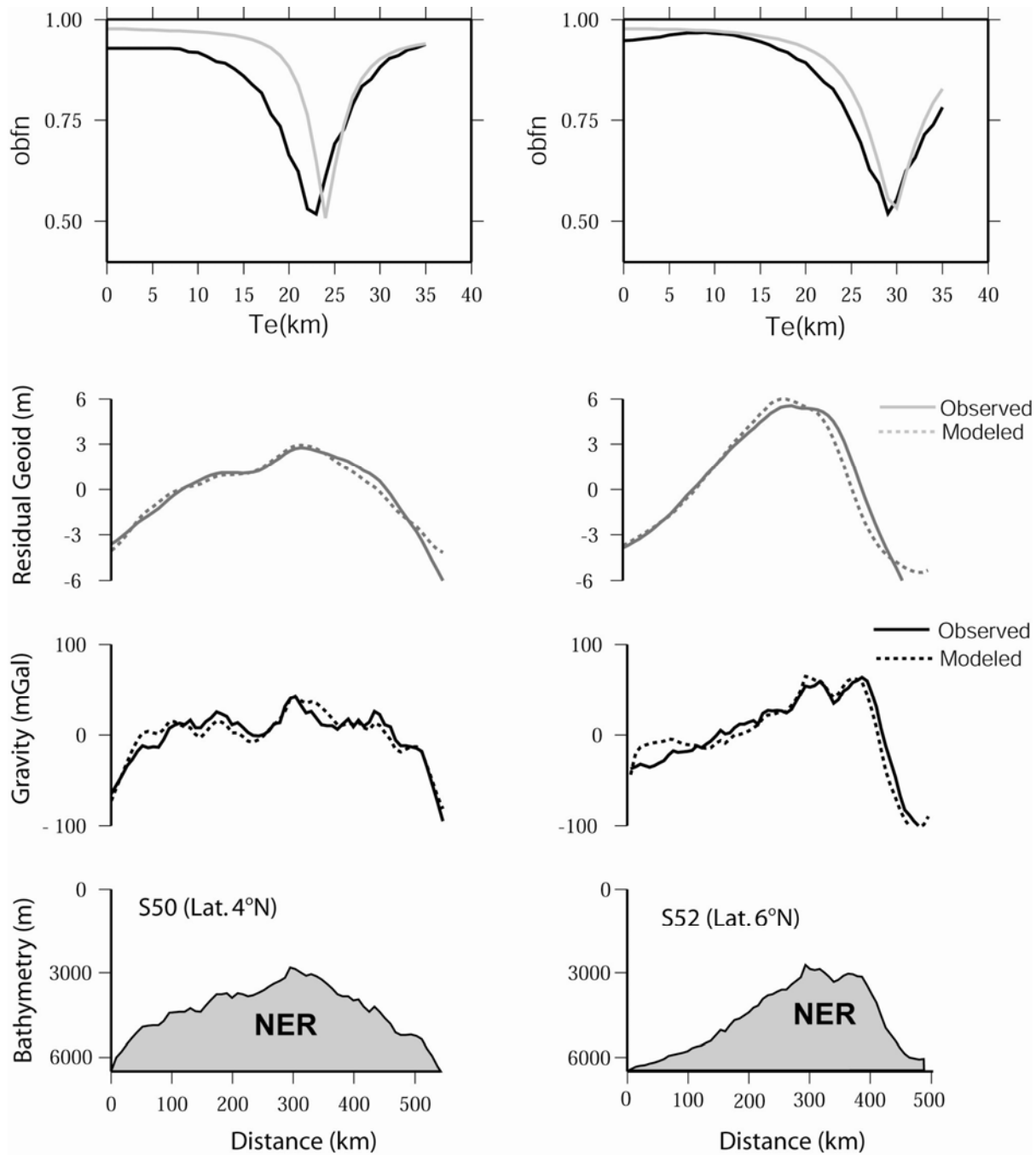


**Figure 6d:** Flexural modeling along selected profiles from the northern part of the Ninetyeast Ridge. Figure format is same as Figure 6a.

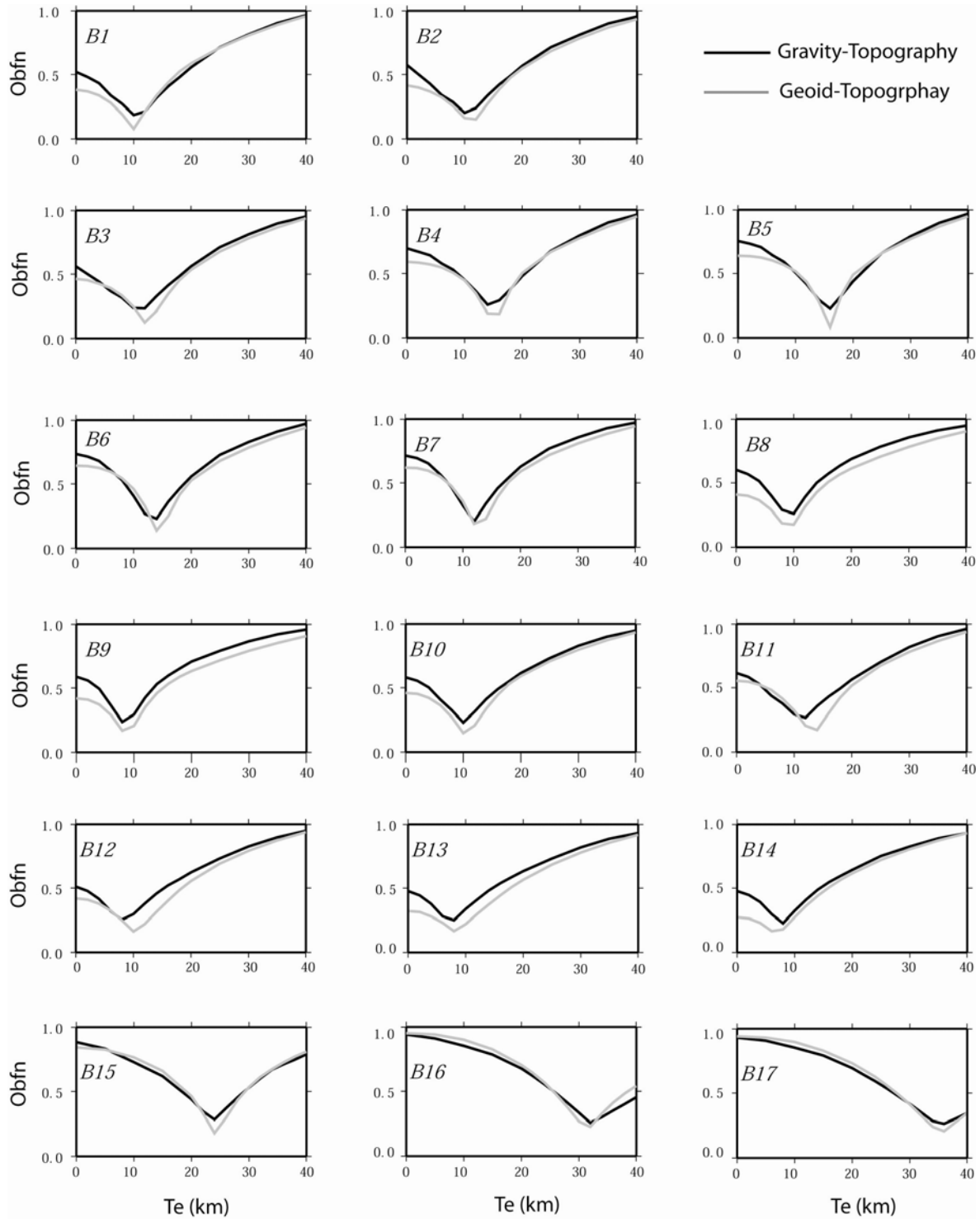


**Figure 7:** Objective function misfit for 3-D flexural modeling of gravity (black) and geoid (gray) along blocks B1-B17. The best fit  $T_e$  with error bounds are listed in Table 3.

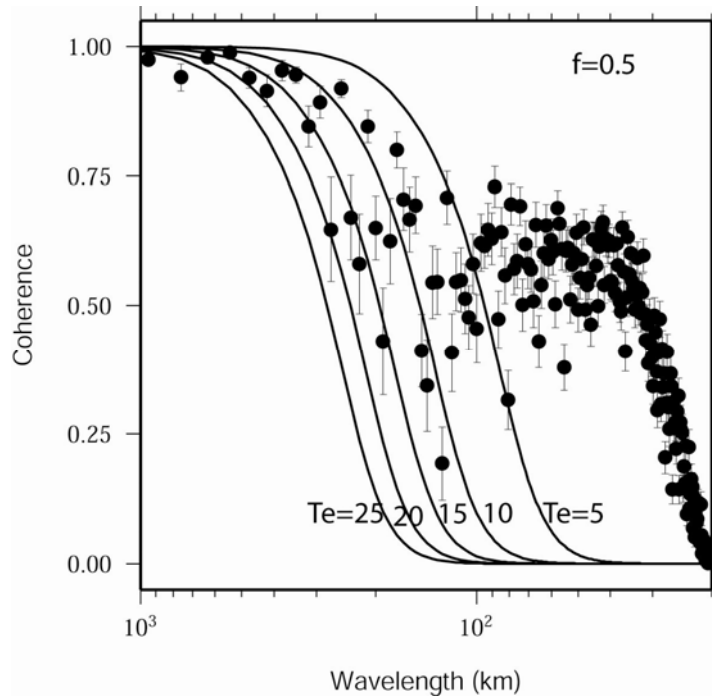


**Figure 8a:** Observed coherence between RMBA data and residual topography of the NER (28°S to equator) with theoretical coherence for  $Te$  values 5 to 25 assuming  $f = 0.5$ .

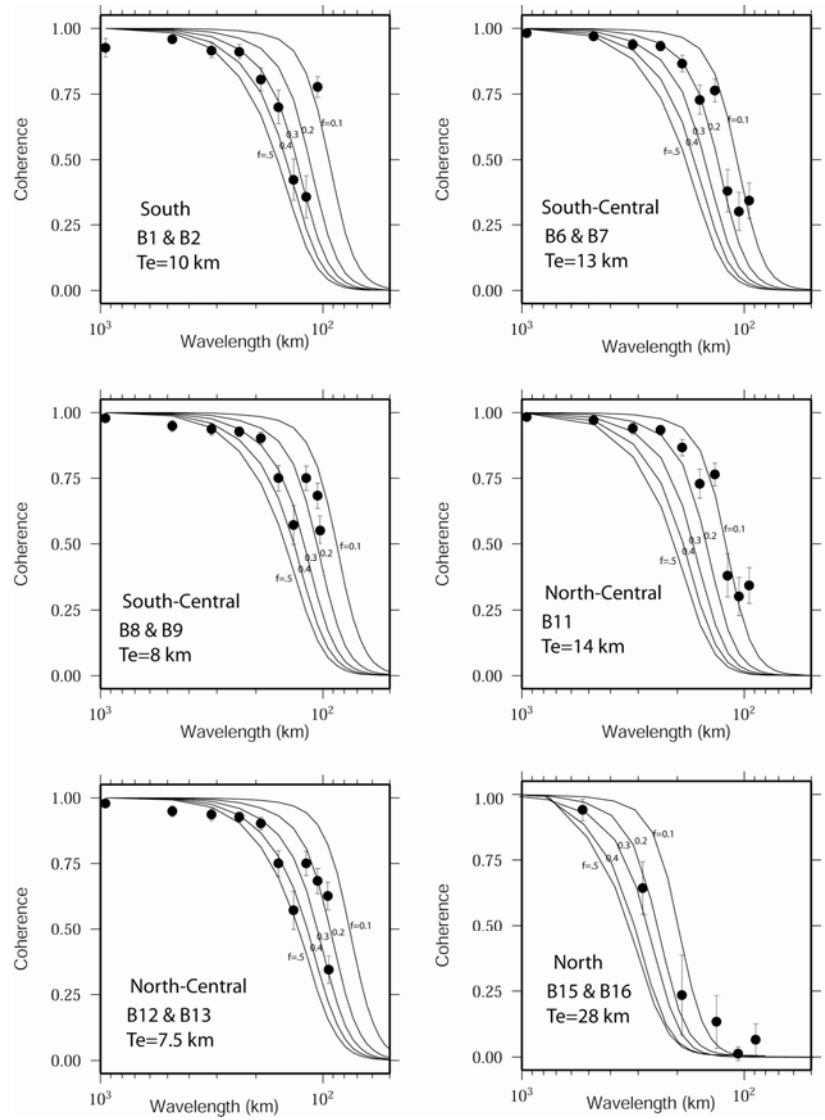


**Figure 8b:** Observed coherence between RMBA data and residual topography of the NER from selected blocks (having close  $T_e$  values) from the southern, south-central, north-central and northern parts of the NER with theoretical coherence for  $f=0.1$  to  $0.5$ .

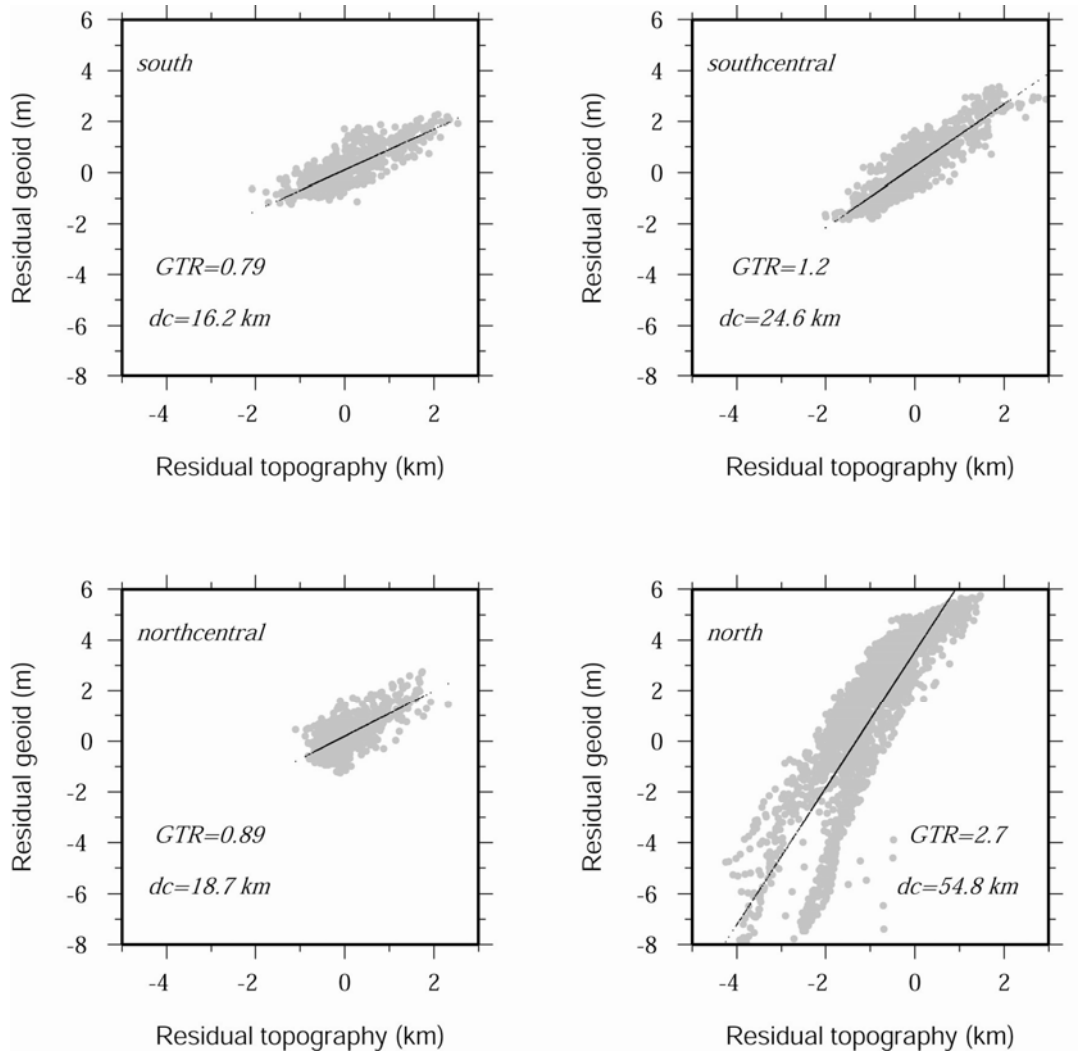


**Figure 9:** Geoid to topography ratio (GTR) and apparent compensation depth (dc) for 4 ridge segments along the NER. The values of GTR and dc for blocks B1-B17 are listed separately in Table 4.

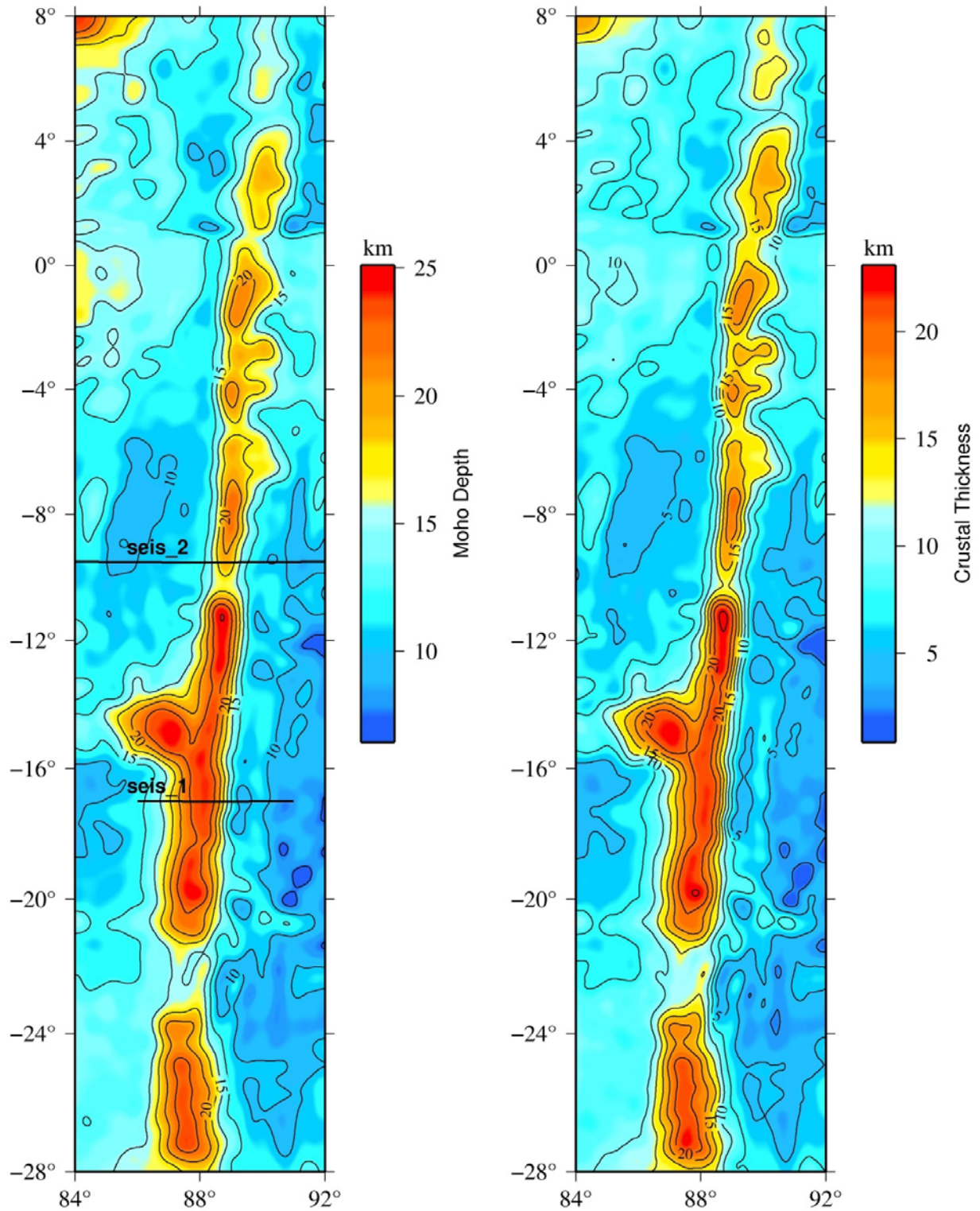


**Figure 10:** Moho topography and crustal thickness maps of the NER obtained from the inversion of RMBA data (Figure 4). Location of OBS profiles seis\_1 (17°S) and seis\_2 (9.5° S) are shown on the Moho topography map.



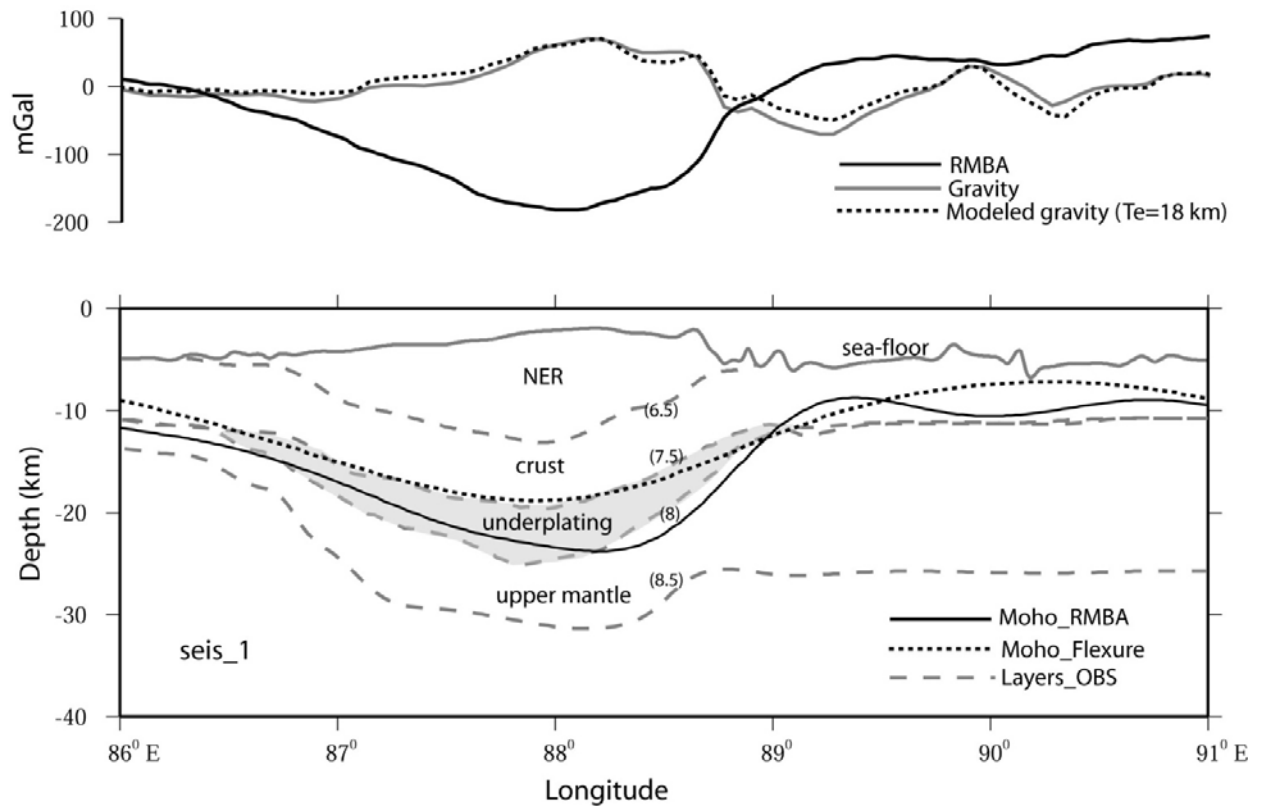


**Figure 11a:** Comparison of Moho topography derived from the inversion of RMBA data and flexural modeling study with the OBS-derived crustal model [Grevymeyer *et al.*, 2001] along seis\_1 (approximately along 17°S latitude).

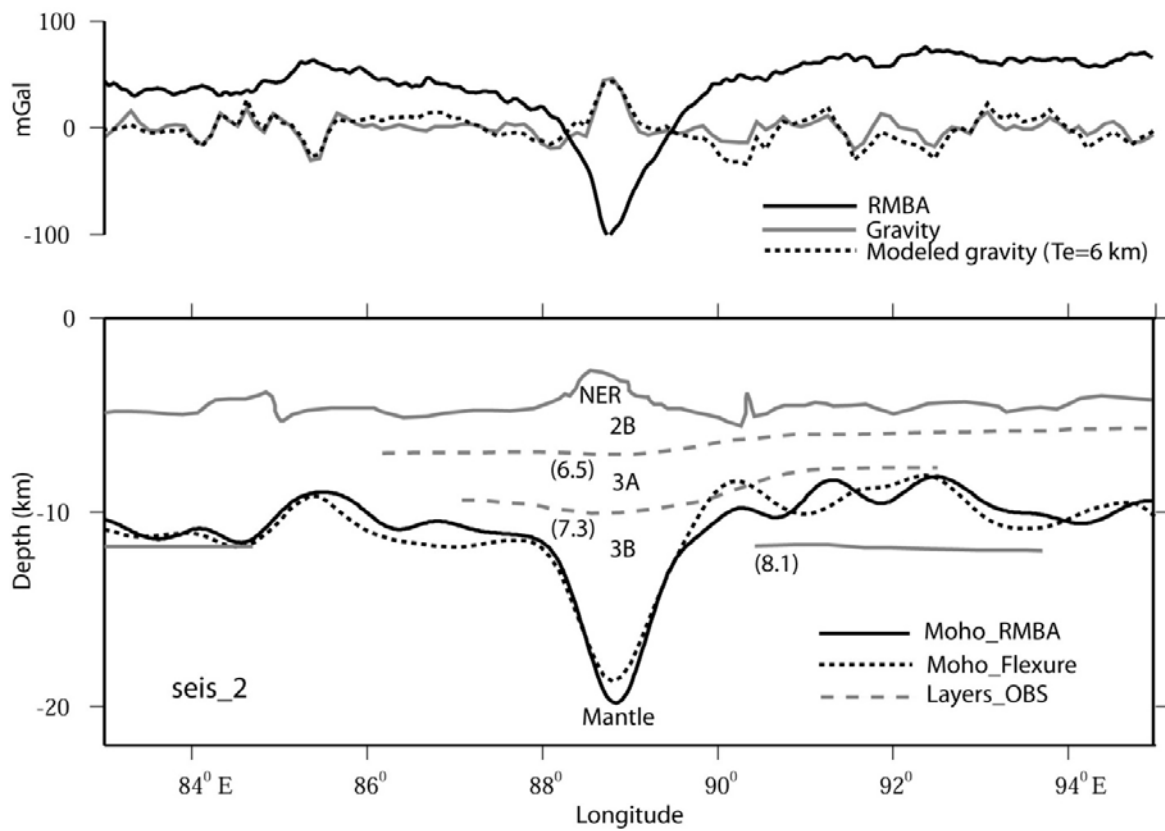


**Figure 11b:** Comparison of Moho topography derived from the inversion of RMBA data and flexural modeling study with the OBS-derived crustal model [Krishna *et al.*, 2001a] along seis\_2 (approximately along 9.5°S latitude).

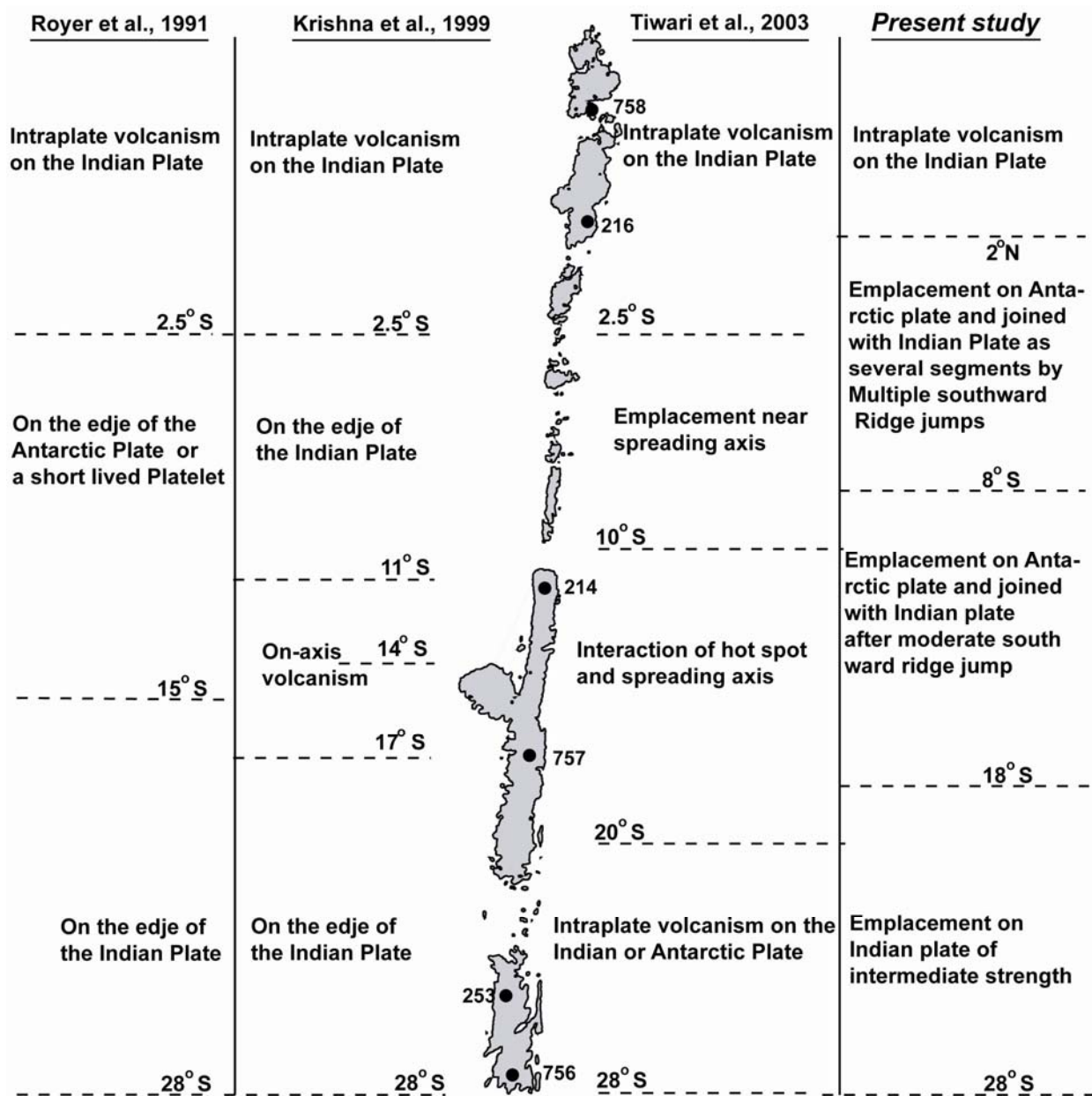


**Figure 12:** Evolutionary model proposed for the accretion of the NER, showing the Kerguelen hot spot location with reference to the Wharton spreading centers. The present model is compared with the existing models [Royer et al., 1991, Krishna et al., 1999; Tiwari et al., 2003].

**Table 1:** Model parameters used for the flexural computations

<i>Parameter</i>	<i>Value</i>
Density of Sea-Water ( $\rho_w$ )	1.03 gm/cc
Density of load ( $\rho$ )	2.6 gm/cc
Density of oceanic crust ( $\rho_c$ )	2.90 gm/cc
Density of mantle( $\rho_m$ )	3.30 gm/cc
Average crustal thickness ( $t$ )	6 km
Young's modulus ( $E$ )	100 Gpa
Poisson's ratio ( $\sigma$ )	0.25
Universal gravitational constant ( $G$ )	$6.67 \cdot 10^{-11} \text{ Nm}^2\text{kg}^{-2}$
Acceleration due to gravity ( $g$ )	$9.8 \text{ ms}^{-2}$

**Table 2:**  $T_e$  values along Ninetyeast Ridge (south to north) obtained by 2D flexural modeling of gravity-topography and geoid-topography data sets

Profile Name	Latitude	$T_e$ (km)					
		Gravity-Topography			Geoid-Topography		
		lower	Best fit	upper	lower	Best fit	upper
S1	-27.5	10	<b>11</b>	14	9.6	<b>9.7</b>	10.3
S2	-27.125	10.6	<b>11</b>	12	9.8	<b>10</b>	10.9
S3	-26.75	12.4	<b>13</b>	13.4	9.5	<b>10</b>	10.3
S4	-26.2	8.5	<b>9</b>	10.5	7.8	<b>10</b>	10.5
V1811	-26	13	<b>14</b>	15	9	<b>12</b>	12.2
S5	-25.5	13.7	<b>14</b>	15.3	11.7	<b>13</b>	13.4
S6	-25	10.15	<b>11</b>	11.8	11.7	<b>12</b>	13.2
S7	-24.5	10.82	<b>12</b>	12.7	10.9	<b>12</b>	12.5
S8	-24	8.7	<b>10</b>	10.6	9.6	<b>10</b>	10.4
S9	-23.5	9	<b>10</b>	11.5	9.6	<b>10</b>	10.4
S10	-23	10	<b>11</b>	12	12.3	<b>13</b>	14.5
S11	-22.5	12	<b>14</b>	15	12.6	<b>14</b>	15
S12	-22	12	<b>13</b>	14	11.5	<b>13</b>	13.5
S13	-21.7	10.6	<b>13</b>	14.1	12.5	<b>13</b>	13.5
DME10	-21	5	<b>6</b>	6.5	5	<b>6</b>	7
S14	-20.5	6.5	<b>8</b>	9	9	<b>10</b>	12
S15	-20	10.3	<b>11</b>	11.8	9.5	<b>10</b>	10.5
S16	-19.5	17.8	<b>19</b>	20.1	16.9	<b>18</b>	19
S17	-19	16.3	<b>17</b>	17.6	14.7	<b>16</b>	16.5
S18	-18.5	18.6	<b>20</b>	20.9	17.2	<b>18</b>	18.5
A20931	-18.19	20.3	<b>21</b>	22.9	17.8	<b>18</b>	20
S19	-17.5	14.8	<b>16</b>	16.9	14.8	<b>16</b>	16.3
S20	-17	18	<b>19</b>	19.5	17.8	<b>18</b>	18.3
S21	-16.5	16.4	<b>17</b>	17.9	13	<b>15</b>	15.7
S22	-16	13.6	<b>14</b>	14.8	12.5	<b>13</b>	15
S23	-15.5	17.5	<b>19</b>	19.5	14.7	<b>15</b>	15.5
S24	-15	18	<b>20</b>	25	16.2	<b>17</b>	17.6
S25	-14.5	14	<b>19</b>	20	19	<b>21</b>	22
S26	-14	11.6	<b>12</b>	16	11.4	<b>12</b>	13.3
S27	-13.5	11.4	<b>12</b>	13.7	10.6	<b>11</b>	11.4
V3305	-13.4	9.6	<b>10</b>	10.6	8.5	<b>10</b>	10.5
S28	-13	11.4	<b>12</b>	13.8	9.2	<b>10</b>	10.5
S29	-12.5	8.7	<b>11</b>	12	10.6	<b>11</b>	11.5
S30	-12	11.6	<b>12</b>	13.8	11.6	<b>12.5</b>	13.4
S31	-11.5	10.3	<b>11</b>	11.3	8.8	<b>10</b>	10.3
V2410	-11	10.7	<b>11</b>	11.7	9.6	<b>12</b>	13.8
p84	-10.6	7.3	<b>8</b>	8.4	4.2	<b>6</b>	6.7
S32	-9.5	7.4	<b>8</b>	9.3	4.5	<b>6</b>	6.6
S33	-9	6.5	<b>7</b>	8.4	5.4	<b>6</b>	6.6
S34	-8.5	6.2	<b>7</b>	10.7	5.3	<b>6</b>	7.1
SK28-1	-7.8	6	<b>7</b>	7.5	3.2	<b>4</b>	8

S35	-7.4	4	<b>5</b>	5.5	4.8	<b>6</b>	6.5
S36	-7	10.7	<b>13.5</b>	14	12.6	<b>13</b>	13.6
SK28-2	-6.6	19.5	<b>20</b>	21	16	<b>17</b>	18.5
V3616	-6	14	<b>15</b>	17	9.9	<b>14</b>	15.9
S37	-5.6	7.9	<b>10</b>	10.6	9.2	<b>10</b>	10.7
V2901	-5.5	19	<b>20</b>	21	16.9	<b>18</b>	18.5
SK28-3	-5	2.5	<b>4</b>	5	6.3	<b>7</b>	7.5
S38	-5	2.4	<b>5</b>	5.8	6.3	<b>7</b>	7.5
S39	-4.6	7	<b>8</b>	8.7	9.2	<b>10</b>	11.6
Chi4	-4	23.6	<b>25</b>	26.1	16	<b>17</b>	18
S40	-4	21.8	<b>24</b>	25.5	18.5	<b>19</b>	21
Sk28-4	-3.9	22	<b>24</b>	25.2	18	<b>19</b>	20.5
S41	-3.4	9.9	<b>11</b>	11.8	12.3	<b>13</b>	14.4
S42	-2.9	8	<b>10</b>	10.9	8.5	<b>10</b>	10.8
Dme7-1	-2.5	3	<b>3.5</b>	4	3.4	<b>4</b>	5
Chi2	-2	3.8	<b>4</b>	5	5.8	<b>6</b>	7.8
V3308	-1.9	4	<b>5</b>	5.6	5.2	<b>6</b>	7.7
S43	-1.5	8.5	<b>9</b>	10.5	9.2	<b>10</b>	10.5
Chi1	-1	20	<b>22</b>	23	17.8	<b>18</b>	19
S44	-0.5	12	<b>14</b>	14.3	10.6	<b>12</b>	12.6
S45	0.75	9.7	<b>11</b>	12	5	<b>6</b>	7
S46	1	14.8	<b>16</b>	17.4	9.5	<b>10</b>	10.5
S47	1.5	8	<b>10</b>	10.6	8	<b>9</b>	10
Dme07-2	2	26	<b>27</b>	28	25.6	<b>26</b>	27.3
S48	2.5	25.5	<b>26</b>	26.5	25.6	<b>26</b>	27.3
S49	3	20.8	<b>22</b>	23.5	21	<b>22</b>	24
S50	4	21.5	<b>23</b>	24	23.8	<b>24</b>	24.23
S51	5	21.5	<b>22</b>	23	28.5	<b>29</b>	31
S52	6	28	<b>29</b>	30	29	<b>30</b>	31
S53	7	31.2	<b>32</b>	34.4	32	<b>34</b>	36
S54	8	27	<b>30</b>	31	26	<b>28</b>	29

**Table 3:**  $T_e$  values along Ninetyeast Ridge (south to north) obtained by 3D flexural modeling using gravity-topography and geoid-topography data sets.

Block Name	Centre Latitude	$T_e$ (km)					
		Gravity-Topography			Geoid-Topography		
		lower	Best fit	upper	lower	Best fit	upper
B1	-25.5	9.8	<b>10</b>	10.5	9.7	<b>10</b>	11
B2	-23.5	9.7	<b>10</b>	10.25	10.7	<b>12</b>	12.2
B3	-21.5	9.8	<b>10</b>	10.6	11.8	<b>12</b>	14
B4	-19.5	13.6	<b>14</b>	15	13.9	<b>15</b>	16
B5	-17.5	15.6	<b>16</b>	17	15.9	<b>16</b>	16
B6	-15.5	11	<b>12</b>	13	13.9	<b>14</b>	14.12
B7	-13.5	11.8	<b>12</b>	13.5	11	<b>13</b>	14
B8	-11.5	7.8	<b>8</b>	10	7.8	<b>8</b>	8.6
B9	-9.5	5.7	<b>8</b>	8.1	7.8	<b>8</b>	8.2
B10	-7.5	9.5	<b>10</b>	10.2	9.8	<b>10</b>	10.2
B11	-5.5	12	<b>13</b>	14	14	<b>15</b>	16
B12	-3.5	7	<b>6</b>	8	6	<b>7</b>	9
B13	-1.5	5	<b>6</b>	7	7.5	<b>8</b>	8.2
B14	0.5	7.7	<b>8</b>	8.3	5.5	<b>6</b>	7
B15	2.5	23.5	<b>24</b>	24.5	23.8	<b>24</b>	24.2
B16	4.5	31.5	<b>32</b>	32.3	28.9	<b>30</b>	33.4
B17	6.5	33.5	<b>36</b>	36.8	34.7	<b>35</b>	35.5

**Table 4:** Results of coherence analysis and geoid to topography ratio analysis of 17 overlapping blocks (B1-B17). The best fit  $T_e$  is the average of  $T_e$  estimations using gravity-topography and geoid topography analysis. For each block, the ratio of sub-surface to surface loading ratio ( $f$ ),  $GTR$  and apparent compensation depths ( $dc$ ) are listed.

<b>Block Name</b>	<b>Centre Latitude</b>	<b>Best fit <math>T_e</math> (km)</b>	<b><math>f</math></b>	<b><math>GTR</math> (m/km)</b>	<b><math>dc</math> (km)</b>
B1	-25.5	10	0.3	0.7945	16.155
B2	-23.5	11	0.3	0.8164	16.6
B3	-21.5	11	0.2	0.9262	18.833
B4	-19.5	14.5	0.2	1.25	25.414
B5	-17.5	16	0.2	1.356	27.556
B6	-15.5	13	0.15	1.3275	26.992
B7	-13.5	12.5	0.2	1.242	25.255
B8	-11.5	8	0.35	1.0393	21.134
B9	-9.5	8	0.5	0.92615	18.8323
B10	-7.5	10	0.35	0.94706	19.2575
B11	-5.5	14	0.2	1.0003	20.34
B12	-3.5	8	0.6	0.9244	18.7967
B13	-1.5	7	0.5	0.8107	16.488
B14	0.5	7	0.5	0.7119	14.4762
B15	2.5	24	0.3	2.1582	43.885
B16	4.5	31	0.35	2.6988	54.877
B17	6.5	35.5	0.3	2.8976	58.91